BRNO UNIVERSITY OF TECHNOLOGY

Faculty of Mechanical Engineering

MASTER'S THESIS

Brno, 2026 Bc. Sára Hrdinová



BRNO UNIVERSITY OF TECHNOLOGY

VYSOKÉ UČENÍ TECHNICKÉ V BRNĚ

FACULTY OF MECHANICAL ENGINEERING

FAKULTA STROJNÍHO INŽENÝRSTVÍ

INSTITUTE OF PHYSICAL ENGINEERING

ÚSTAV FYZIKÁLNÍHO INŽENÝRSTVÍ

MODIFICATION OF FERH THIN FILMS FOR MAGNETIC STORAGE APPLICATIONS

MODIFIKACE TENKÝCH VRSTEV FERH PRO APLIKACE V MAGNETICKÉM ZÁZNAMU

MASTER'S THESIS

DIPLOMOVÁ PRÁCE

AUTHOR — **Bc. Sára Hrdinová**

AUTOR PRÁCE

SUPERVISOR — **Ing. Vojtěch Uhlíř, Ph.D.**

VEDOUCÍ PRÁCE

BRNO 2026

BRNO UNIVERSITY OF TECHNOLOGY
FACULTY OF MECHANICAL ENGINEERING

Master's Thesis Assignment

Institute:	Institute of Physical Engineering
Student:	**Bc. Sára Hrdinová**
Degree programm:	Physical Engineering and Nanotechnology
Branch:	no specialisation
Supervisor:	**Ing. Vojtěch Uhlíř, Ph.D.**
Academic year:	2025/26

As provided for by the Act No. 111/98 Coll. on higher education institutions and the BUT Study and Examination Regulations, the director of the Institute hereby assigns the following topic of Master's Thesis:

Modification of FeRh thin films for magnetic storage applications

Brief Description:

FeRh is a CsCl–type alloy that undergoes a first–order antiferromagnetic–ferromagnetic transition near 370 K, accompanied by lattice expansion and changes in resistivity and entropy. In thin films, this transition shows thermal hysteresis, tunable for applications. Optimizing hysteresis and shifting the transition toward room temperature can be achieved through tuning the deposition parameters and thin film composition. This can be extended to varying film thickness and substrate to tune the strain state of the films. Additionally, ion irradiation and implantation will be used to modify the composition and amount of defects in the films.

Master's Thesis goals:

1. Evaluate the effect of deposition parameters, film thickness, and substrate on the phase transition characteristics
2. Modify the phase transition parameters by controlled ion irradiation
3. Evaluate the ferromagnetic phase distribution in the depth profile of the films

Recommended bibliography:

BENITO, L.; CLARK, Laura; TREVOR P. ALMEIDA; T. A. MOORE; MCGROUTHER, D. et al. Sputter-engineering a first-order magnetic phase transition in sub-15-nm-thick single-crystal FeRh films. Physical Review Materials. 2020, vol. 4, no. 12. ISSN 2475-9953. DOI: 10.1103/physrevmaterials.4.123402.

STEVEN P. BENNETT; HERKLOTZ, Andreas; CORY D. CRESS; ANTON V. IEVLEV; CHRISTOPHER M. ROULEAU et al. Magnetic order multilayering in FeRh thin films by He-Ion irradiation. Materials Research Letters. 2017, vol. 6, no. 1, s. 106-112. ISSN 2166-3831. DOI: 10.1080/21663831.2017.1402098.

Deadline for submission Master's Thesis is given by the Schedule of the Academic year 2025/26

In Brno,

L. S.

prof. RNDr. Tomáš Šikola, CSc. Director of the Institute	doc. Ing. Jiří Hlinka, Ph.D. FME dean

Abstrakt

Fázová přeměna prvního řádu z antiferomagnetické (AF) do feromagnetické (FM) fáze v ekviatomických slitinách FeRh vzbudila zájem díky potenciálním aplikacím v technologiích magnetického záznamu a paměťových technologiích. K přeměně dochází mírně nad pokojovou teplotou, typicky kolem 350 K, a vykazuje tepelnou hysterezi o šířce přibližně 20 K, během které koexistují AF a FM fáze. Vysoká laditelnost FeRh spolu s výraznými změnami magnetizace a elektrického odporu, které doprovázejí fázovou přeměnu, činí tento materiál obzvláště zajímavým. Provoz paměťových zařízení, které by využívalo FeRh s běžnou teplotou přeměny by však vyžadoval vnější ohřev, který je energeticky nevýhodný. Navíc relativně úzký interval koexistence fází omezuje tepelnou stabilitu zařízení. Pro technologické aplikace je proto žádoucí snížit teplotu přeměny k 300 K a zároveň podstatně rozšířit tepelnou hysterezi. V této práci je zkoumána laditelnost fázové přeměny v tenkých vrstvách FeRh optimalizací podmínek depozice a následným ozařováním ionty C^+ a H^+ s energií 20 keV. Studie se zaměřuje na řízení teploty přeměny T_t a šířky hystereze ΔT prostřednictvím změn tloušťky vrstvy, typu substrátu, dávky iontů a teploty ozařování. Výsledky ukazují, že vrstvy s tloušťkou 20 nm deponované na Al_2O_3 mají již po depozici tepelnou hysterezi o šířce 58 K, jejíž střed se nachází blízko pokojové teploty. Ozařování ionty C^+ vede k výraznému rozšíření přeměny, které dosahuje až 84 K, doprovázenému snížením T_t až na 227 K. Ozařování ionty v kombinaci s žíháním navíc umožňuje posunutí teplotní hystereze vzorků s původně vysokými hotnotami T_t směrem k pokojové teplotě s šířkou hystereze kolem 50 K.

Summary

The first order phase transition from the antiferromagnetic (AF) to the ferromagnetic (FM) phase in equiatomic FeRh alloys has attracted interest due to its potential applications in magnetic recording and memory technologies. The transition occurs slightly above room temperature, around 350 K, and exhibits a thermal hysteresis with a width of approximately 20 K, within which the AF and FM phases coexist. The high tunability of FeRh, together with the pronounced changes in magnetization and electrical resistivity accompanying the phase transition, makes this material particularly attractive. However, practical operation of the potential magnetic storage device utilizing common FeRh films would require external heating, which reduces energy efficiency. In addition, the relatively narrow phase coexistence interval limits the thermal stability of the device. For technological applications, it is therefore desirable to both decrease the transition temperature toward 300 K and to substantially broaden the thermal hysteresis. In this work, we investigate the tunability of the phase transition in FeRh thin films by optimizing deposition conditions and by subsequent irradiation with C^+ and H^+ ions with the energy of 20 keV. The study focuses on controlling the transition temperature T_t and the hysteresis width ΔT through variations in film thickness, substrate type, ion dose, and irradiation temperature. The results show that 20-nm-thick FeRh films grown on Al_2O_3 exhibit, already in the as-grown state, a thermal hysteresis 59 K wide centered near room temperature. Irradiation with C^+ ions leads to a pronounced broadening of the transition, reaching up to 84 K, accompanied by a significant reduction of T_t down to 227 K. Furthermore, ion irradiation combined with annealing enables shift of the thermal hysteresis of samples with initially high T_t close to room temperature with hysteresis widths of around 50 K.

Klíčová slova
Feromagnetismus, Antiferomagnetismus, FeRh, Fázová přeměna, iontové ozařování, VSM, MFM, RBS, PNR, fázové domény, teplotní hystereze, teplota přeměny, zbytková magnetizace

Keywords
Ferromagnetism, Antiferromagnetism, FeRh alloy, Phase transition, ion irradiation, VSM, MFM, RBS, PNR, phase domain, thermal hysteresis, transition temperature, residual magnetization

HRDINOVÁ, S.*Modifikace tenkých vrstev FeRh pro aplikace v magnetickém záznamu.* Brno: Vysoké učení technické v Brně, Fakulta strojního inženýrství, 2026. 61 s. Vedoucí .

Rozšířený abstrakt

Fázová přeměna prvního řádu z antiferomagnetické (AF) do feromagnetické (FM) fáze v ekviatomických slitinách FeRh vzbudila zájem díky potenciálním aplikacím v technologiích magnetického záznamu a paměťových technologiích. K přeměně dochází mírně nad pokojovou teplotou, typicky kolem 350 K. Přeměna je doprovázena tepelnou hysterezí o šířce přibližně 20 K, v jejímž rozsahu koexistují AF a FM fáze. Vysoká laditelnost FeRh spolu s výraznými změnami magnetizace a elektrického odporu, které doprovázejí fázovou přeměnu, činí tento materiál obzvláště zajímavým. Přeměna je vysoce citlivá na vnější magnetická pole, deformaci, chemické složení a mřížkové defekty [1, 2]. I malé lokální deformace mřížky mohou posunout teplotu přeměny T_t a iniciovat nebo oddálit nukleaci fázových domén [1, 3, 4].
Předchozí studie ukázaly, že teplotu T_t lze posunout o více než 100 K pomocí dopování [5] nebo iontového ozařování [6]. Tepelnou hysterezi lze ovlivnit řadou parametrů, ke kterým patří například podmínky během depozice [7], typ substrátu [8], složení [9] a tloušťka vrstvy FeRh [10]. Kromě teploty přeměny je teplotní hystereze popsána také šířkou hystereze a zbytkovou magnetizací. Zbytková magnetizace M_{res} kvantifikuje feromagnetické oblasti vrstvy FeRh, které zůstávají ve feromagnetickém uspořádání v celém teplotním rozsahu a nepřecházejí do AF fáze. Tento zbytkový feromagnetický příspěvek může být rozložen po celé vrstvě FeRh, nebo lokalizován na rozhraní se substrátem, jak bylo dříve pozorováno [7, 11]. Pro většinu aplikací je zbytková magnetizace nežádoucí. Obzvláště u ultratenkých vrstev FeRh s tloušťkami menšími než 15 nm, kde M_{res} může představovat více než 50 % [12]. V praktických zařízeních na bázi FeRh, zejména v oblasti magnetického ukládání dat, by proto měla být hodnota M_{res} minimalizována. Provoz zařízení využívajících běžné vrstvy FeRh při pokojové teplotě často vyžaduje externí ohřev, což snižuje jejich energetickou účinnost. Relativně úzký interval koexistence fází dále omezuje tepelnou stabilitu zařízení. Je tedy žádoucí snížit teplotu přeměny směrem k 300 K, rozšířit tepelnou hysterezi a udržet zbytkovou magnetizaci na nízké hodnotě.
V rámci této práce byla zkoumána laditelnost fázové přeměny v tenkých vrstvách FeRh optimalizací podmínek depozice a následným ozařováním ionty C^+ a H^+ o energii 20 keV. Studie je zaměřena na optimalizaci teploty přeměny T_t, šířky hystereze ΔT a zbytkové magnetizace prostřednictvím změn tloušťky vrstvy, typu substrátu, dávky iontů a teploty ozařování. Pozornost byla věnována také hloubkovému profilování zbytkové magnetizace a nukleaci fázových domén, protože tyto veličiny poskytují vhled do lokálního chování přeměny a jsou přímo spojeny s parametry tepelné hystereze.
První část práce je zaměřena na možnost ladění tenkých vrstev FeRh během jejich přípravy. Výsledky ukazují, že substrát má výrazný vliv na teplotu přeměny. Vrstvy deponované na substrát z Al_2O_3 vykazují systematicky nižší T_t než vrstvy nanesené na substrát MgO. Toto chování je v souladu s indukovanou epitaxní tahovou deformací způsobenou substrátem Al_2O_3, která stabilizuje FM fázi a posouvá přeměnu směrem

k nižším teplotám. Současně má substrát z Al_2O_3 tendenci rozšiřovat teplotní hysterezi. Tloušťka FeRh představuje další laditelný parametr. Zmenšení tloušťky FeRh obecně vede ke snížení T_t a k rozšíření hystereze. Tento trend nelze vysvětlit pouze epitaxním napětím a souvisí také s efekty konečné tloušťky vrstvy, které mohou snížit teplotu přeměny a přispět k rozšíření hystereze.
Reprodukovatelnost parametrů teplotní přeměny je silně ovlivněna napětím vrstvy. Srovnání vzorků připravených s použitím různých svorek k uchycení substrátu naznačuje, že i mechanické upevnění substrátu během depozice může významně ovlivnit tepelnou hysterezi. Spolehlivé ladění vlastností FeRh během depozice proto vyžaduje nejen stejný substrát a tloušťku vrstvy FeRh, ale také pečlivou kontrolu upevnění vzorku a napětí během růstu. Vhodným vzorkem získaným optimalizací depozičních parametrů byla vrstva FeRh o tloušťce 20 nm, deponovaná na substrátu Al_2O_3 při tlaku Ar $2{,}7 \times 10^{-3}$ mbar. Tento vzorek vykazoval přeměnu blízkou pokojové teplotě s $T_t = 312$ K, šířkou tepelné hystereze $\Delta T = 59$ K a zbytkovou magnetizací $M_{res} = 15$ %.
Kromě optimalizace depozice jsme následně ladili tepelnou hysterezi iontovým ozařováním. Ozařování ionty C^+ se ukázalo jako účinný způsob k rozšíření hystereze. Maximální šířka hystereze dosáhla $\Delta T = 84$ K. Toto rozšíření však bylo doprovázeno výrazným poklesem teploty přeměny až na $T_t = 227$ K a nárůstem zbytkové magnetizace až na 40 %. Výběrem vhodné dávky ozařování bylo možné dosáhnout tepelné hystereze nacházející se blízko pokojové teploty s šířkou 56 K. Ozařování při zvýšené teplotě a žíhání po ozařování poskytly alternativní přístupy k optimalizaci hystereze. Tyto metody snížily nadměrný pokles T_t a dostatečně zachovaly rozšíření hystereze, které dosahovalo přibližně 50 K. Vliv ozáření závisel nejen na dávce iontů, ale také na počátečních parametrech tepelné hystereze vzorku. Vzorky s odlišnými počátečními teplotami přeměny vykazovaly po ozáření ionty C^+ s energií 20 keV a totožnou dávkou různou míru rozšíření hystereze. To naznačuje, že účinek iontového ozáření nelze posuzovat nezávisle na počátečním stavu.
Byl zkoumán také vliv iontového ozáření ionty H^+ s energií 20 keV. Ve srovnání s ozářením uhlíkem byly k vyvolání srovnatelné změny fázové přeměny potřeba podstatně vyšší ozařovací dávky vodíku. To je v souladu s jeho nižší hmotností a menší pravděpodobností rozptylu. Ozařování vodíkem vedlo ke snížení teploty přeměny o 35 K, ke zvýšení šířky hystereze o 23 K a ke zvýšení zbytkové magnetizace o 20 %. Došlo také ke zvýšení celkové magnetizace ve ferromagnetické fázi, které bylo potvrzeno pomocí vibrační vzorkové magnetometrie a polarizované neutronové reflektometrie. Měření mikroskopie magnetických sil ukázalo, že ozářený vzorek obsahoval větší počet nukleačních zárodků s menší velikostí. To naznačuje, že ozáření mohlo zpomalilo růst fázových domén, což by mohlo vysvětlovat rozšíření tepelné hysterezní smyčky pozorované po ozařování.

I declare that I have written my master's thesis on the topic of *Modification of FeRh thin films for magnetic storage applications* independently, under the guidance of my supervisor, Ing. Vojtěch Uhlíř, Ph.D., and using the sources quoted in the list of literature at the end of the thesis. This work was created with help of ChatGPT and Gemini generative AI models, which were used for text formatting and grammatical corrections.

Bc. Sára Hrdinová

First and foremost, I would like to express my gratitude to Vojtěch Uhlíř for his guidance throughout my work, inspiring advice and consultations. I am also very grateful to Jon Ander Arregi Uribeetxebarria for providing characterized samples. I greatly appreciate his willingness and proactive support.
I would also like to thank Daniel Primetzhofer for facilitating the measurements in Tandem laboratory and my stay at Uppsala University, Alexey Dobrynin for consultations and advice on simulations. I would also like to thank Mauricio Sortica for his help with ion irradiations, André Vantomme and Radek Holeňák for their help with ion analysis and Alexey Vorobiev for help with polarized neutron reflectometry measurements at Institut Laue–Langevin.
CzechNanoLab project LM2023051 funded by MEYS CR is gratefully acknowledged for the financial support of the measurements/sample fabrication at CEITEC NanoResearch Infrastructure.
Velmi děkuji také své rodině a příteli za nenahraditelnou podporu během celého studia.

Bc. Sára Hrdinová

Contents

Introduction **3**

1 First-order phase transition in FeRh **5**
1.1 Thermal hysteresis . . . 7
1.2 Tunability of thermal hysteresis . . . 9
1.2.1 Influence of strain . . . 9
1.2.2 Influence of magnetic field . . . 11
1.2.3 Influence of rhodium composition . . . 11
1.2.4 Influence of doping . . . 13
1.2.5 Influence of lattice defects . . . 13
1.3 Phase domain nucleation . . . 14
1.4 FeRh applications . . . 16
1.4.1 Exchange-spring-coupled heterostructure for HAMR . . . 17
1.4.2 Robust antiferromagnet-based memory resistor . . . 18
1.4.3 Voltage-controlled storage memory . . . 18
1.4.4 Requirements on thermal hysteresis . . . 18

2 Tunability upon deposition **21**
2.1 Chemical composition . . . 23
2.2 Effect of substrate . . . 27
2.3 Effect of FeRh layer thickness . . . 27
2.4 Additional source of strain . . . 30
2.5 Optimal deposition conditions . . . 33

3 FeRh ion irradiation **35**
3.1 C^+ irradiation . . . 37
3.1.1 Dose dependence . . . 39
3.1.2 Irradiation at elevated temperature . . . 40
3.2 C^+ and N^+ irradiation . . . 41
3.3 H^+ irradiation . . . 42
3.4 Localization of the residual magnetization . . . 43
3.5 Phase-domain evolution after H^+ irradiation . . . 46

Conclusions **53**

Bibliography **57**

Introduction

The first order phase transition from the antiferromagnetic (AF) to the ferromagnetic (FM) phase in equiatomic FeRh alloys has attracted renewed interest due to its potential applications in magnetic recording and memory technologies. The transition occurs slightly above room temperature, around 350 K, and exhibits a thermal hysteresis with a width of approximately 20 K, within which the AF and FM phases coexist. The high tunability of FeRh, together with the pronounced changes in magnetization and electrical resistivity accompanying the phase transition, makes this material particularly attractive. The transition is highly sensitive to external magnetic fields, strain, chemical composition, and defects [1, 2]. Even small local lattice distortions can shift the transition temperature T_t and initiate or delay phase domain nucleations [1, 3, 4]. It was already shown, that the transition temperature T_t can be effectively adjusted by more than 100 K using doping [5] or irradiation [6]. Change of deposition parameters [7], substrate [8], composition [9] or layer thickness [10] influence not only the T_t, but also alters other thermal hysteresis features, like width of the hysteresis or residual magnetization. The residual magnetization quantifies ferromagnetic regions of the FeRh layer that remain FM over the entire temperature range and never transition into AF phase. This fraction can be present around defects, uniformly in the layer, or as was earlier confirmed, at the interface with the substrate [7, 11].

The residual magnetization in majority of the application creates unwanted magnetic fields, which becomes crucial especially for ultrathin FeRh (sub-15-nm-thick) films, where the residual magnetization may account for 50 % or more of its magnetization in the FM phase [12]. For the practical operation of real world applications in magnetic data storage, this residual magnetization has to be minimized. Moreover, operation of the device near room temperature typically requires external heating, which reduces energy efficiency. In addition, the relatively narrow phase coexistence interval limits its thermal stability. Thus, for technological applications, it is desirable to both decrease the transition temperature toward 300 K and to substantially broaden the thermal hysteresis.

The underlying mechanisms behind the formation of residual magnetization, hysteresis broadening and phase nucleation remain unexplained, therefore within this work, we investigate the behavior and tunability of the phase transition in FeRh thin films by optimizing deposition conditions and by subsequent irradiation with C^+ and H^+ ions with the energy 20 keV. The study focuses on controlling the transition temperature T_t, the hysteresis width ΔT and residual magnetization M_res through variations in film thickness, substrate type, ion dose, and irradiation temperature. An attention is also

given to the depth profiling of the residual magnetization and phase domain nucleation, since it provides insight into the local transition behavior and directly correlates with the thermal hysteresis parameters.

1. First-order phase transition in FeRh

The properties of FeRh depend strongly on its chemical composition, temperature, and sample preparation. The FeRh phase diagram shown in Fig. 1.1 provides an overview of the stable phases as a function of rhodium concentration and temperature. In terms of crystal structure and magnetic ordering, several distinct phases can be identified. At high temperatures below the liquidus curve, FeRh crystallizes either in a paramagnetic (PM) chemically disordered γ phase with a face-centred cubic (FCC) lattice or in a PM chemically disordered δ phase with a body-centred cubic (BCC) structure. At lower temperatures and lower rhodium concentrations, an α phase is stabilized. This phase exhibits a chemically disordered BCC lattice and a ferromagnetic (FM) ordering. With increasing Rh concentration above approximately 10 %, a new phase α' becomes stable, which retains the BCC-based structure and shows a FM ordering with partial chemical ordering. Finally, within a narrow composition range of approximately 48 % to 55 % Rh, a unique α'' phase appears. This nearly equiatomic phase is characterized by a chemically ordered CsCl-type lattice and an antiferromagnetic (AF) spin arrangement, which undergoes a first-order metamagnetic phase transition [2, 13]. The phase transition was first observed in 1938 [14] and has since been the subject of numerous publications [2].

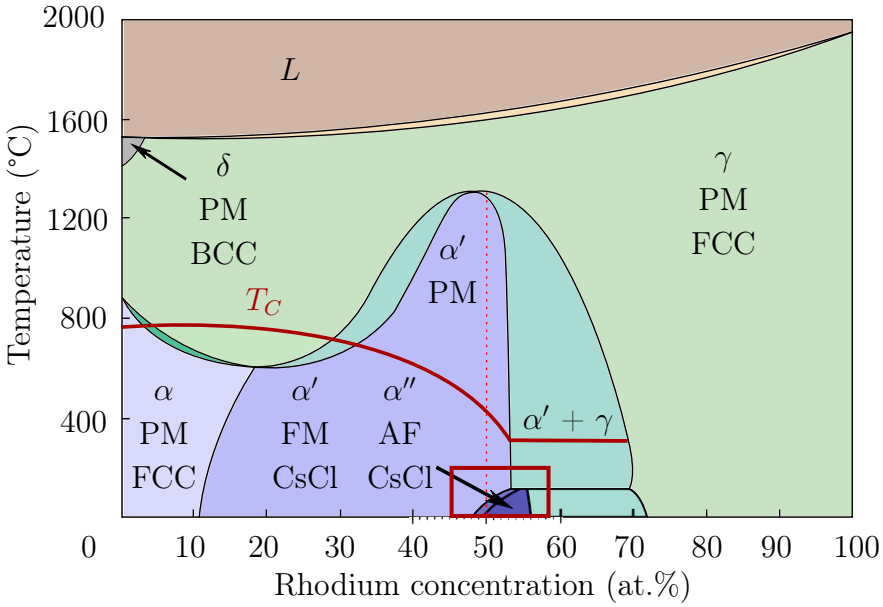


Figure 1.1: Phase diagram of FeRh, displaying magnetic ordering and lattice structure of each phase with a highlighted region of interest, where the phase transition from antiferromagnetic (AF) to ferromagnetic (FM) order takes place. Adapted from [13].

The first-order metamagnetic phase transition in FeRh takes place slightly above room temperature (around 350 K) [3]. During this transition, the lattice expands [15] and the magnetic order changes from AF to FM, which results in pronounced changes in resistivity and magnetization [3], as shown in Fig. 1.2. First principles band structure calculations revealed that the α'' phase has an energy minimum in the AFII configuration. Very close in energy lies the minimum of the α' phase, that has FM spin configuration and a lattice parameter approximately 0.5 % larger [16]. The AF α'' phase is governed primarily by nearest-neighbour Fe–Fe exchange interactions. On the other hand the FM α' is mediated by longer-range interaction of Rh atoms between neighbouring Fe sites, leading to stabilization of the FM order of Fe atoms and polarization of the magnetic moment of Rh [17].

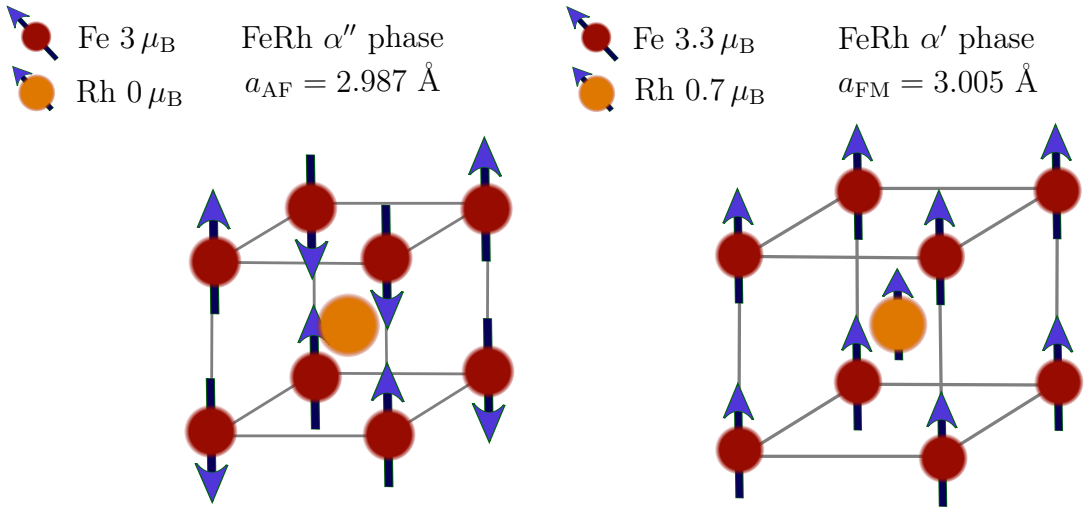


Figure 1.2: Lattice structure and magnetic ordering of the antiferromagnetic AFII α'' phase and the ferromagnetic α' phase in FeRh. The configuration of magnetic moments on Fe and Rh sites and their respective orientations are illustrated. Adapted from [18].

The connection between the lattice parameter and the magnetic ordering is well known. However, despite many years of research, the trigger of the transition remains a matter of debate. Some measurements suggest that the expansion of the lattice changes the magnetic ground state, other studies claim that the thermodynamic phase transition in the magnetic system occurs before the lattice expands. The possible driving mechanism could be expansion-induced change of the exchange constant [19] or excitation of spin waves [20]. This ambiguity was the main subject of the article [21], that used atomistic spin dynamics and pump-probe laser experiments. It is again shown the nearest Fe-Fe neighbors favor the AF spin order and the Rh moment, in this case included in nonlinear higher-order exchange terms, is responsible for the FM ordering. Their results suggest that changes in the magnetic order precede lattice expansion, although this claim cannot still be conclusively proven and remains an open question.

1.1 Thermal hysteresis

A defining characteristic of a first-order phase transition is the existence of an energy barrier between the competing phases, which necessitates the absorption or release of latent heat during the transition [1, 3]. Due to this barrier, the system does not transition immediately upon reaching the equilibrium temperature, but requires further heating or cooling to overcome the metastable state. This delay results in thermal hysteresis, where the transition temperatures during heating and cooling differ [1, 3], as illustrated in Fig. 1.3. Thermal hysteresis can be characterized by several key parameters, namely the transition temperature T_t, the hysteresis width ΔT, and the residual magnetization M_{res}.

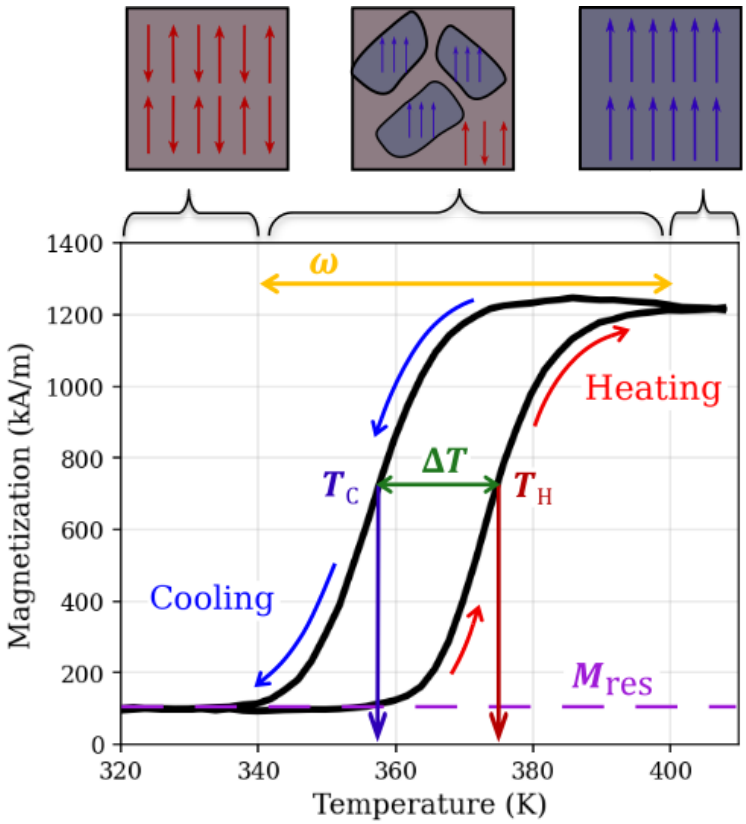


Figure 1.3: Temperature dependence of magnetization illustrating the first-order phase transition in FeRh. The increase in magnetization during heating and the subsequent decrease during cooling define the thermal hysteresis loop. Key parameters as the transition temperatures during heating (T_h) and cooling (T_c), the hysteresis width (ΔT), the transition width (w) and the residual magnetization (M_{res}) are indicated. The schematic above the graph depicts the the phases, including their coexistence.

The transition temperature T_t is commonly defined as the average of the transition temperatures during heating T_h and cooling T_c. These characteristic temperatures, T_h and T_c, are identified as the inflection points of the respective the hysteresis loop branches. At these points, the slope of the magnetization curve reaches its maximum, representing the temperature at which the phase transition proceeds at the highest rate per unit of temperature.

Another parameter is the hysteresis width ΔT, that is given by the difference of the transition temperatures $T_h - T_c$ and corresponds to the temperature change needed to overcome the intrinsic energy barrier between the phases [10]. However, in reality we measure the global thermal hysteresis, that is a combination of local loops. Therefore broad distribution of local transition temperatures, caused by structural defects or local strain variations (that are further discussed in section 1.2), prevents the entire film from transitioning at once. This leads to a decrease in the transition rate per unit of temperature and might deform the shape of the thermal hysteresis. It can influence not only the hysteresis width, but also the nucleation temperature onset and the phase transition completion. Hence another parameter, the transition width w is sometimes defined. It represents the maximum temperature interval in which both the AF and FM phases can coexist. A large w indicates a broader distribution of local transition temperatures and slow transition rate per temperature unit. In other words, the transition width w is a signature of the material's heterogeneity, while the hysteresis width ΔT measures the global energy barrier. However, these parameters might be interconnected.

At low temperatures, the magnetization of FeRh is theoretically expected to be zero in the AF state due to the perfect compensation of individual magnetic moments. In practice, the magnetization remains non-zero because some regions retain their FM character and do not undergo the transition. These regions are quantified by the residual magnetization M_{res}. This parameter can be defined either as the minimum magnetization observed in the AF state at low temperatures or as the percentage of the saturation magnetization M_{sat}, which represents the maximum magnetization achieved in the fully FM phase at high temperatures. This ratio $M_{\text{res}}/M_{\text{sat}}$ serves as a critical indicator of the phase purity and the degree of B2 crystalline order within the FeRh film. Origin of M_{res} is typically attributed to chemical gradients resulting in a disordered α' phase, γ phase or the presence of crystallographic defects that disrupt the periodic AF structure, thereby stabilizing FM order. A key aspect of investigating M_{res} is its spatial localization, since it can be distributed both laterally and vertically within FeRh films. The majority of the residual magnetization originates from a stabilized FM interfacial layer at the substrate interface. This residual FM phase limits the fabrication of ultrathin FeRh layers. Therefore, its origin and possible elimination are the subject of current research. Previous studies have shown that M_{res} can be reduced by optimizing the sputtering pressure for films of different thicknesses [7, 12, 22].

The origin of the ferromagnetic interface can be attributed either to chemical disorder, as a strong correlation between the residual magnetization and the chemical order parameter has been reported [22, 11], or to a compositional gradient arising from diffusion. This diffusion may be driven by interfacial strain gradients [11] and enhanced at elevated temperatures, for example during annealing. These hypotheses have been further supported and elaborated in the literature. Electron energy-loss spectroscopy (EELS) analysis revealed an approximately 1.5 nm-thick Fe-rich interfacial layer in sub-10 nm films after annealing above 600 °C [22]. Recent structural investigations combining scanning transmission electron microscopy (STEM) and EELS have further confirmed the diffusion of Fe atoms into the MgO substrate during deposition and subsequent

annealing, providing the current picture of interfacial M_{res} formation. The diffusion of Fe into the MgO substrate resulting in a relative Rh enrichment of the interfacial FeRh region was reported in [23]. The Rh enrichment led to the formation of a chemically inhomogeneous, Rh-rich γ phase with a disordered FCC structure, extending over approximately 1–5 monolayers. This interfacial layer exhibits a substantial lattice mismatch with respect to MgO ($\approx 11\,\%$), which results in local stress relaxation and the formation of dislocations. In combination with Fe–O hybridization, the presence of this structurally distinct phase modifies the electronic density of states at the interface and thereby suppresses the AF–FM transition locally at the interface.

1.2 Tunability of thermal hysteresis

The transition is highly sensitive to external magnetic fields, strain, chemical composition, and defects [1, 2]. Even small local lattice distortions can initiate nucleation of phase domains [1, 3, 4]. As a result, the magnetization often increases gradually with temperature rather than exhibiting a sharp, abrupt transition. Let's now take a closer look at these mechanisms.

1.2.1 Influence of strain

One of the most effective ways to control the thermal hysteresis and the transition temperature T_{t} is through strain. The underlying principle is illustrated in Fig. 1.4. Compressive strain suppresses the lattice expansion accompanying the transition, thereby stabilizing the AF phase and increasing T_{t}. In contrast, tensile strain facilitates lattice expansion and stabilizes the FM phase, resulting in a reduction of T_{t}.
A shift of T_{t} can be achieved through different sources of strain. For example, piezoelectric substrates, whose lattice parameters can be tuned by an applied voltage, enable reversible control of the magnetic phase and of T_{t} [24]. Another important source of strain is the lattice mismatch between the film and the substrate. This mismatch can be quantified by a in-plane epitaxial strain ϵ_x, defined as

$$\epsilon_x = \frac{a_{\mathrm{s}} - a}{a}, \tag{1.1}$$

where a_{s} denotes the lattice parameter of the substrate and a is the in-plane lattice parameter of the film. By substituting the $a_{\mathrm{FeRh}} = 2.987$ Å and

$$a_{\mathrm{MgO}} = \frac{\sqrt{2}}{2} \times 4.216\ \text{Å} \approx 2.978\ \text{Å}, \tag{1.2}$$

we obtain the nominal epitaxial strain $\epsilon_x = -0.3\,\%$ of the FeRh lattice grown on a MgO substrate (Fig. 1.5a).
The corresponding lattice distortion is shown in Fig. 1.5b. In this case, the compressive epitaxial strain imposed by the MgO substrate contracts the in-plane lattice parameters, while the lattice expands along the out-of-plane direction z. Since the out-of-plane lattice parameter c can be readily determined by X-ray diffraction (XRD), the out-

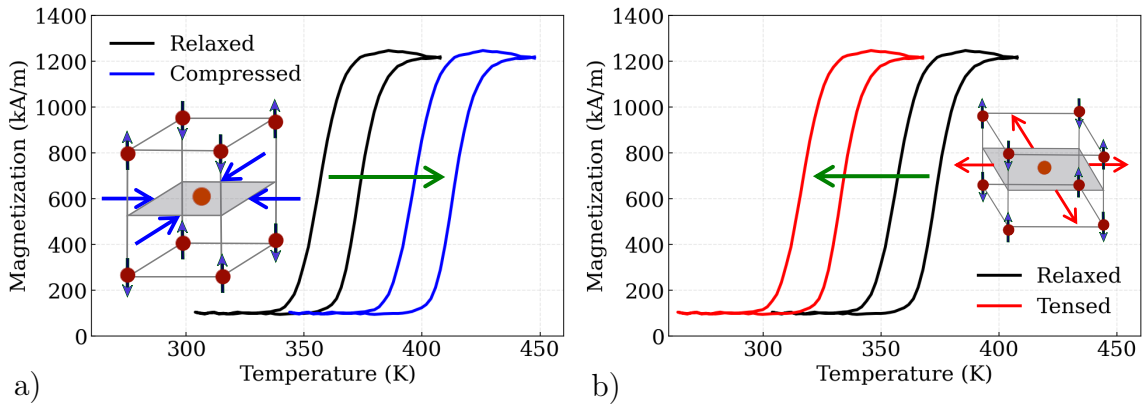


Figure 1.4: Schematic representation of the transition temperature T_t shift induced by strain. (a) Compressive in-plane strain opposes the volume expansion accompanying the transition, thereby stabilizing the antiferromagnetic phase and shifting T_t to higher temperatures. (b) In-plane tensile strain, which facilitates the lattice expansion, promoting the ferromagnetic phase and shifting T_t to lower temperatures.

of-plane strain ϵ_z can be evaluated with respect to the relaxed bulk lattice parameter $a_0 = 2.987$ Å as

$$\epsilon_z = \frac{c - a_0}{a_0}. \tag{1.3}$$

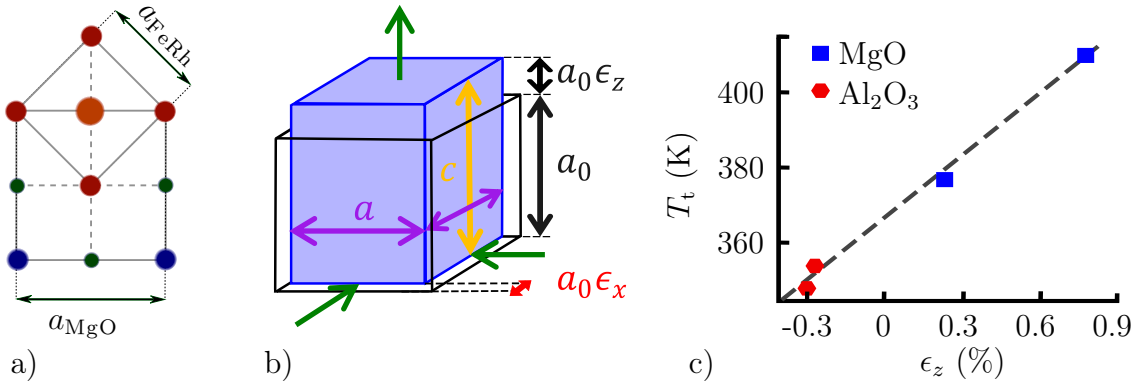


Figure 1.5: (a) Schematic illustration of the FeRh lattice accommodated to MgO substrate. (b) Representation of the lattice deformation parameters after application of strain along the x and y directions. (c) Linear dependence of the transition temperature T_t on strain for 50-nm-thick FeRh films grown on MgO and Al_2O_3 substrates. Adapted from [25].

A difference in T_t of approximately 20 K has been reported for FeRh films grown on Al_2O_3, which imposes an epitaxial strain of approximately 11.3 %, and on MgO, where the epitaxial strain is about −0.3 % [8, 25]. The influence of epitaxial strain is further demonstrated by removing the substrate, which leads to a pronounced decrease in T_t [26]. The dependence of T_t on strain is approximately linear, as shown in Fig. 1.5c. In particular, the compressive strain imposed by MgO results in a negative in-plane strain

ϵ_x, which is accompanied by an out-of-plane expansion corresponding to a positive ϵ_z and an upward shift of T_t.

1.2.2 Influence of magnetic field

The application of an external magnetic field $\mu_0 H$ shifts the transition temperature T_t toward lower values, as the field stabilizes the FM phase with a higher magnetic moment. For nearly equiatomic FeRh layers grown on a MgO substrate, this shift is approximately -8 to $-9\,\mathrm{K\,T^{-1}}$ [27, 28].

1.2.3 Influence of rhodium composition

The importance of chemical composition was emphasized at the beginning of this chapter. The phase diagram shown in Fig. 1.1 illustrates not only the narrow compositional range in which the AF phase is stable, but also the increase in the T_t with increasing Rh concentration in bulk FeRh. In thin films, however, the situation is more complex. In addition to composition, several other parameters influence the phase transition, including film thickness, epitaxial strain, interfacial effects (such as oxidation, roughness, and atomic diffusion), and the quality of epitaxial growth during deposition.
For example, 100-nm-thick FeRh films grown on MgO exhibit a crystallographic phase evolution consistent with the bulk phase diagram, whereas the composition dependence of T_t shows an opposite trend [9]. As the Rh concentration increases from 35 % to 47 %, the out-of-plane lattice parameter c gradually increases from 2.977 Å to 3.07 Å (Fig. 1.6b), while the magnetic moment increases from approximately 1400 kA/m to 1600 kA/m. Significant changes are also observed in the chemical order parameter S (defined by equation 1.2.5), which increases from 0.6 to 0.9 (Fig. 1.6a). This improvement in chemical ordering is attributed to the composition approaching the equiatomic FeRh stoichiometry. At a Rh concentration of 47 %, the first thermal hysteresis and signatures of AF ordering are observed. Increasing the Rh concentration to 48 % leads to an abrupt decrease of the lattice parameter to 2.99 Å, which is associated with the appearance of the ordered α'' phase. With further increase in Rh content, the lattice parameter again increases approximately linearly, reaching 3.02 Å at 55 % Rh, while the chemical order remains constant throughout this composition range. For Rh concentrations above 55 %, an additional XRD peak corresponding to the γ phase is observed, which is characteristic of Rh-rich films. These observations are consistent with the phase diagram, where the chemically disordered α' phase is expected for Rh deficient compositions, whereas the γ phase appears in Rh-rich alloy.
Overall, the lattice parameter exhibits an approximately linear increase with increasing Rh concentration, interrupted only by the abrupt change associated with the formation of the AF α'' phase, and the measured crystallographic parameters are consistent with the expectations given by phase diagram [9]. However, the T_t appears to decrease with increasing Rh content (Fig. 1.6c), in contrast to the trend expected from the bulk phase diagram. At the same time, both the hysteresis width ΔT and the transition width w increase with increasing Rh concentration. These changes appear to origi-

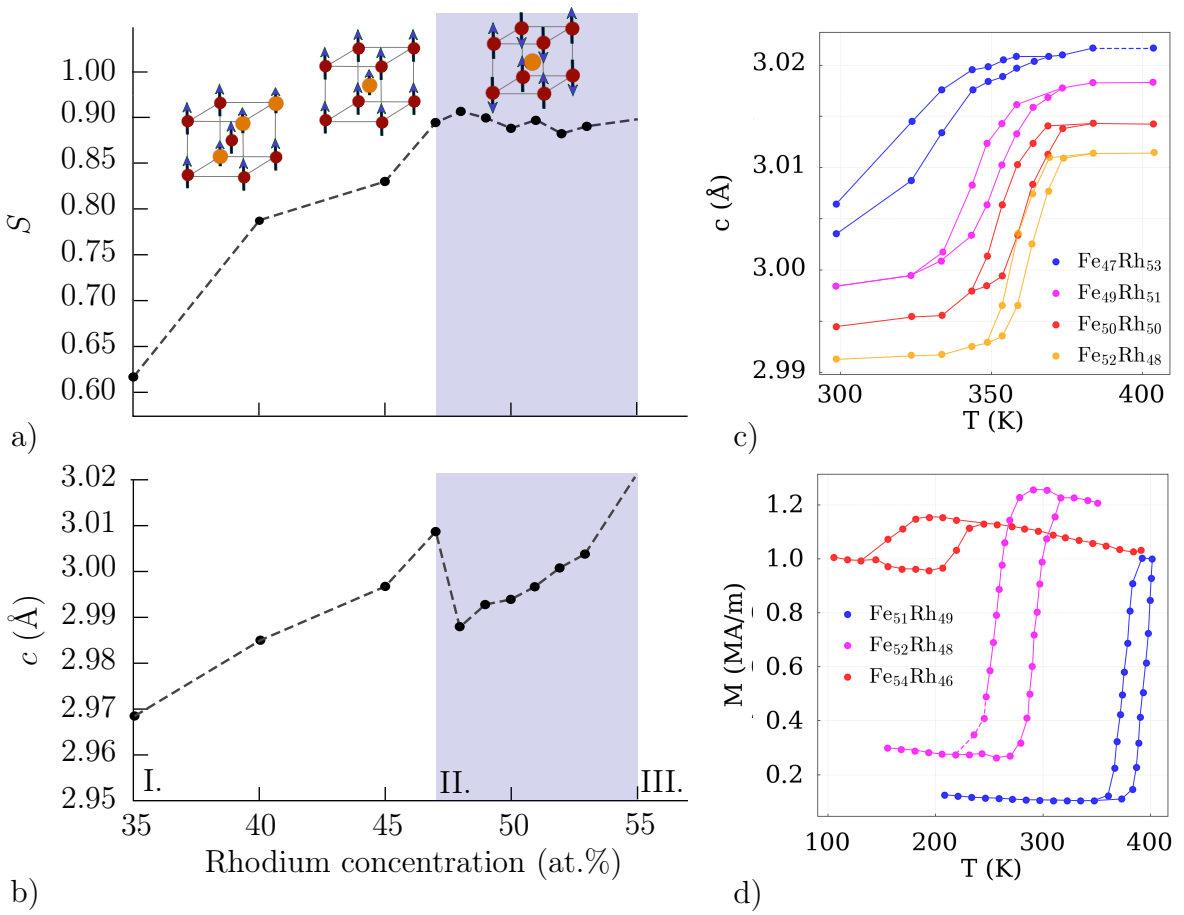


Figure 1.6: (a) A gradual improvement of chemical order described by the order parameter S in 100-nm-thick FeRh films grown on MgO. (b) Out-of-plane lattice parameter c as a function of rhodium concentration. In the region II. an antiferromagnetic α'' phase appears. (c) Thermal hysteresis of films with different Rh concentrations illustrated by the temperature dependence of c. Panels (a)–(c) are adapted and modified from Ref. [9]. (d) Thermal magnetic hysteresis of 25-nm-thick FeRh films with different Rh concentrations, adapted and modified from Ref. [29].

nate primarily from an upward shift of the low temperature onset of the transition, while the high temperature completion of the transition remains nearly unchanged for all compositions. This behavior may reflect the influence of defects and local inhomogeneities that broaden the distribution of local transition temperatures [9], as discussed in Section 1.2.

The Rh composition can also be tuned by adjusting the argon deposition pressure during sputtering [29]. For 25-nm-thick FeRh films grown on MgO, increasing the Ar pressure increased the Rh content from 46 % to 50 %, resulting in a pronounced increase of T_t from 225 K to 380 K (Fig. 1.6d). The authors interpret this trend in accordance with the FeRh phase diagram, where increasing Rh concentration stabilizes the AF α'' phase at higher temperatures. However, the measured values of T_t in thin films significantly exceed those reported for bulk material, which is likely related to epitaxial strain that further stabilizes the AF state. Simultaneously, the M_{res} is suppressed with increasing Rh content, which the authors attribute to possible suppression of the FM

α' phase [29].
Based on bulk behavior, slight variations in the Rh concentration are expected to shift the T_t by tens of Kelvin. In thin films, however, these composition induced changes of T_t are often masked by other mechanisms with stronger effects, such as epitaxial strain or defects. Nevertheless, increasing Rh concentration generally leads to an increase in both the transition temperature T_t and the lattice parameter, while the residual magnetization M_{res} tends to decrease.

1.2.4 Influence of doping

Besides the FeRh stoichiometry, the thermal hysteresis is also strongly influenced by doping with a third element. Depending on the choice of dopant, the T_t can shift by more than 100 K. A comprehensive study [5] identified a systematic correlation between T_t and the average number of valence electrons per atom in the resulting ternary compound. This relationship allows an approximate estimate of the change in T_t as a function of both the dopant (Fig. 1.7) species and its concentration.

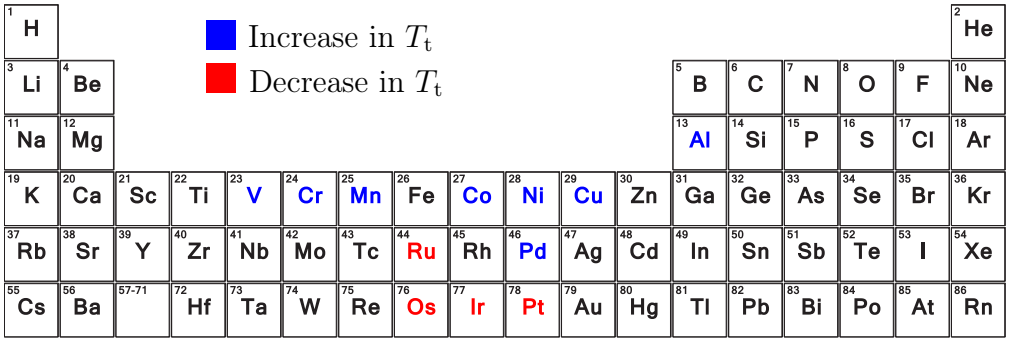


Figure 1.7: An overview of the elements and their effect on the shift in the transition temperature T_t adapted from [5]. The effect of Cu doping was added from [30].

However, this approach does not fully explain all experimentally observed trends. For example, the pronounced reduction of T_t induced by Cu doping, investigated in Ref. [30], cannot be understood solely within this framework. The authors suggested, based on the Hume–Rothery rules, that Cu atoms preferentially substitute Fe rather than Rh atoms. This interpretation is supported by XRD analysis, where the observed shift of diffraction peaks corresponds to lattice enlargement, whereas substitution of Rh would be expected to contract lattice. The incorporation of Cu therefore strongly perturbs the regularity of the AF arrangement and can reduce T_t by more than 100 K.
It is also important to note that the lattice position of the dopant may depend on the deposition method, for example whether the films are prepared from a ternary target or by co-sputtering, as well as on the subsequent annealing procedure.

1.2.5 Influence of lattice defects

The ambiguities in the composition dependent shift of T_t discussed in the previous subsection (Section 1.2.3) already suggest that chemical composition alone is not sufficient

to fully describe the phase transition, espetially for thin films. An important role is played not only by composition itself, but also by the atomic arrangement within the lattice. This crystallographic structure can be modified by defects such as vacancies, atomic substitutions, and interstitial atoms, which thus influence the thermal hysteresis. They can locally modify strain, disrupt the periodicity required for AF ordering, and alter the electronic structure. In general, defects tend to shift the energetic balance toward the ferromagnetic state.
A particularly important factor is the presence of Fe antisite defects [31]. Antisite defects are point defects in which atoms occupy the incorrect sublattice within the ordered CsCl structure of FeRh. In the ideal crystal, Fe and Rh atoms occupy separate sublattices. In real materials, however, finite preparation temperature, atomic diffusion, and limited ordering kinetics inevitably lead to a small degree of atomic exchange. The degree of chemical ordering is commonly described by the order parameter S, which is defined as

$$S = r_A + r_B - 1, \tag{1.4}$$

where r_A and r_B denote the fractions of A and B sites occupied by the correct atomic species, respectively. The order parameter is equal to one for a perfectly ordered lattice, while typical experimental values for FeRh thin films reach around $S \approx 0.9$. According to calculations from the publication [31], even concentration of approximately 2 % of the detrimental Fe antisite defects (in which Fe atoms occupy sites of the Rh sublattice) cause a pronounced reduction of the T_t by more than 130 K. This strong effect originates from the fact that Fe atoms occupying the Rh sublattice carry local magnetic moments and form strong ferromagnetic exchange interactions with neighboring Fe atoms. As a consequence, the delicate balance of competing electronic interactions that stabilizes the AF phase is strongly perturbed. At concentrations of approximately 4 % Fe antisite defects, the phase transition disappears completely [31].
These calculations also suggest that Rh-rich compositions should generally exhibit greater stability of the AF phase. A higher Rh content reduces the probability of Fe atoms occupying the Rh sublattice and therefore suppresses the formation of destabilizing Fe antisite defects. This may help explain why the compositional range from 48 to 55 % Rh, in which the α'' phase appears, is not symmetrically centered around $Fe_{50}Rh_{50}$. As a result of Rh enrichment, the electronic interactions responsible for stabilizing the AF state are better preserved and the transition temperature increases. According to the calculations reported in Ref. [31], the predicted transition temperature is 549 K for $Fe_{48}Rh_{52}$ and 340 K for $Fe_{50}Rh_{50}$, while for $Fe_{52}Rh_{48}$ the phase transition disappears completely.

1.3 Phase domain nucleation

The phase transition and hysteretic behavior is typically characterized from the global point of view by measurements of resistivity, magnetization or crystalographic lattice changes. The resulting signal corresponds to a large sample area. Imaging methods like magnetic force microscopy (MFM) or Kerr Microscopy enable to observe the transition

locally and image individual phase domains nucleation.
The nucleation of phase domains is illustrated in Figure 1.8, where we can see the formation of phase domains during heating and cooling. Nucleation occurs at preferred sites upon repeated thermal cycling, which suggests the transition is governed by heterogeneous nucleation. The activation energy can be explained within the framework of nucleation theory. The key relation is given by

$$\Delta G_b = f \cdot \Delta G_H, \tag{1.5}$$

where ΔG_b is the activation energy for heterogeneous nucleation (i.e., nucleation at defects), ΔG_H is the activation energy for homogeneous nucleation in a perfect crystal, and f is a geometrical factor that depends on the nature of the defect (for example, the character and orientation of grain boundaries). Since real samples contain a distribution of defects with different geometries, each nucleation site is characterized by a different value of f and thus a different activation energy [32].
A crucial distinction must be made between local and global observations of the phase transition. On a local scale, when focusing on an individual nucleation site (of the size of a single nucleus), the transition is very sharp, occurring within a narrow temperature range of less than $\sim 10\,\mathrm{K}$ (and possibly as small as $\sim 5\,\mathrm{K}$ after accounting for instrumental broadening) [32]. In contrast, the macroscopic transition measured over the entire sample appears gradual. This is because the global magnetization curve represents an average over a large number of such local transitions, each occurring at slightly different temperatures due to variations in the local defect structure. As a consequence, the phase nuclei do not form simultaneously but instead appear over a finite temperature interval, leading to increase in transition width.
The phase transition itself proceeds in three basic stages: (i) the formation of nucleation sites for the new phase, (ii) their growth, and (iii) their subsequent coalescence into larger domains. What is more, a pronounced asymmetry between heating and cooling transitions is frequently observed. This can be visible either in the thermal hysteresis or in the phase propagation [33]. The nucleation centers during heating and cooling differ, which could be caused by different nature of defects. For example in patterned nanostructure, the FM nucleation centers are stabilized at the edges. This could be either because of increase of chemical disorder [34] or compressive epitaxial strain relaxation at the edges of patterned nanostructure [35]. However the edges of dewetted areas, which induce compressive strains, serve as nucleation centers for the AF phase [4]. Additionally, AF domains nucleate preferentially at crystallographic defects with very little domain growth. In contrast, the heterogeneous nucleation of the FM phase is then followed by significant growth of the domains [32],[10].

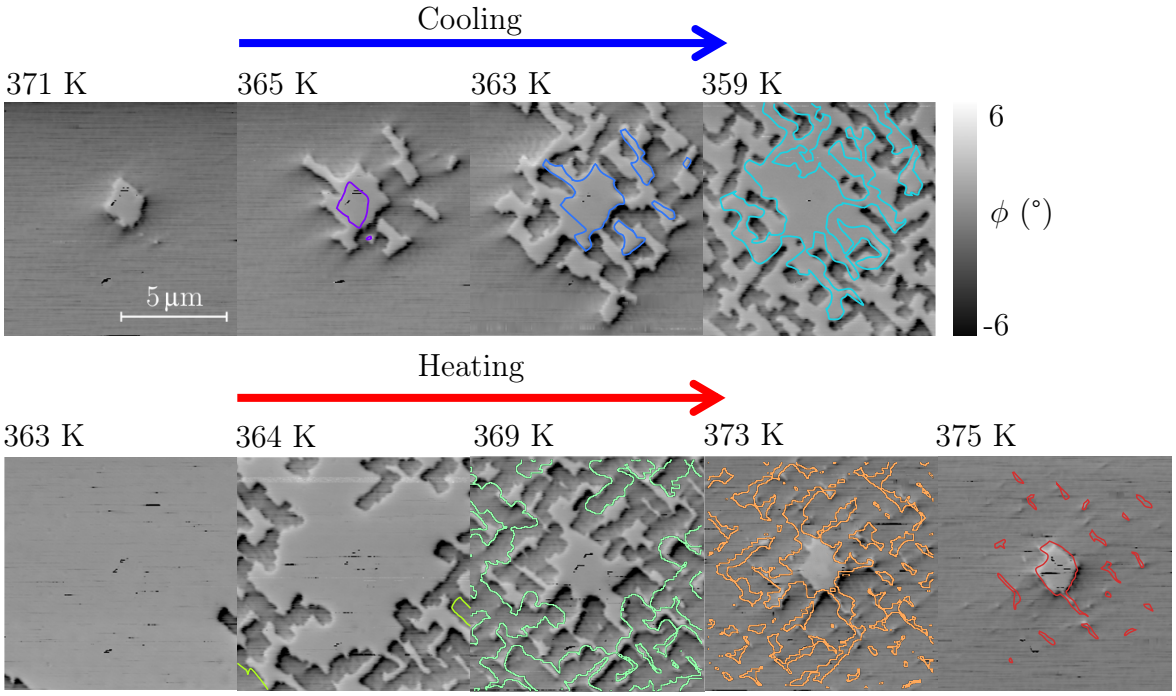


Figure 1.8: Nucleation, growth and merging of antiferromagnetic phase domains during cooling and ferromagnetic phase domains during heating. Colored regions display the phase domain boundaries at previous temperature step. Adapted from [33].

Phase domain growth preferentially occurs along the principal crystallographic axes of FeRh. This behaviour arises from elastic adaptation to substrate-induced strain and from laterally heterogeneous strain distributions associated with the different unit-cell volumes of the coexisting AF and FM phases [4]. Application of an external magnetic field also influences the propagation of phase domains, as demonstrated in the publication [4], where the preferred direction of domain growth was found to align with the applied magnetic field. Besides the direction of nucleation, the depth profile of the individual domains could also affect thermal hysteresis. The question remains whether the phase domains extend through the entire thickness, or whether nucleation begins at the surface or at the interface with the substrate. The paper [36] examined a 56-nm-thick layer and concluded, through calculations and time dependencies of the magnetization measurements, that domains first form on the surface of the layer and then gradually penetrate into the film.

1.4 FeRh applications

Due to its reversible transition, pronounced electronic and magnetic contrast, and tunability by multiple external stimuli, FeRh is attractive for applications in magnetic random-access memory (MRAM), heat-assisted magnetic recording (HAMR), and energy-efficient spintronic devices. The demand for magnetic recording technologies is rapidly increasing with the growing amount of generated and stored data, creating pressure to improve power efficiency, speed, and storage capacity.
Despite the expected gradual phase-out of hard disk drives (HDDs) and their replace-

ment by solid-state drives (SSDs), which has already occurred in many mobile phones and personal computers, the demand for HDDs has recently increased again. This demand is driven mainly by the growth of data associated with artificial intelligence. The computations themselves are performed using fast processors, dynamic random-access memory (DRAM), and SSDs, however, large archives of input data, such as videos, text datasets, medical images, and backups of generated results, are often stored on HDDs. HDDs therefore remain difficult to replace in large-scale archival storage, mainly because of their substantially lower cost per unit of stored data and the high cost of expanding SSD production capacity. In some market segments, the price per unit of HDD storage remains several times lower than that of SSD storage. The largest manufacturers (Seagate, Western Digital) report that their production for 2026 is already sold out, creating pressure to expand production and develop new recording technologies [37, 38].

FeRh has been proposed as a functional material for heat-assisted magnetic recording (HAMR), especially in FeRh/FePt exchange-spring media, where the thermally induced AF–FM transition of FeRh can assist the switching of a hard magnetic FePt layer. Further possible applications of FeRh in data storage include robust antiferromagnet-based memory resistors, where information could be stored in the orientation of the AF Néel vector with negligible stray fields, and voltage-controlled hybrid memory.

1.4.1 Exchange-spring-coupled heterostructure for HAMR

The development of magnetic recording has long been limited by the competing requirements of areal density, writability, and thermal stability. Increasing the areal density requires a reduction of the magnetic grain volume. However, for a constant magnetocrystalline anisotropy, smaller grains become more susceptible to thermal fluctuations, which can lead to a loss of long-term stability. This can be compensated by increasing the anisotropy of the recording medium, but this in turn requires a higher write-field strength, which is limited by the of available write-head materials. These mutually competing requirements form the magnetic recording trilemma, which cannot be overcome without additional energy assistance [39].

One of the approaches to this problem is HAMR, in which a highly anisotropic medium is locally heated by a laser pulse during the writing process. The temporary temperature increase reduces the switching field to a value accessible by the write head. After writing, the medium cools back to ambient temperature, restoring its high magnetic anisotropy and therefore its stability. However, the elevated temperatures reached during HAMR introduce an additional constraint in media design. In addition to grain size, anisotropy, and write-field strength, the written state can become vulnerable to thermally activated backswitching [40].

Despite many challenges in its development, HAMR-based HDDs are now commercially available. FeRh was proposed already two decades ago as a possible improvement for thermally assisted magnetic recording media [41]. The proposed concept consists of a soft ferromagnetic FeRh layer in its high-temperature phase exchange-coupled to a hard ferromagnetic FePt layer. This bilayer structure combines the high magnetocrystalline

anisotropy and Curie temperature of FePt, which provide long-term stability, with the thermally switchable magnetic state of FeRh, which can improve writability through the exchange-spring effect [41].

1.4.2 Robust antiferromagnet-based memory resistor

This application utilizes field cooling of a FeRh layer from the FM state in an applied external magnetic field. After cooling below the transition temperature, the FeRh layer returns to the AF state, while the selected orientation of the Néel vector is retained. This magnetic configuration can then be read electrically through antiferromagnetic anisotropic magnetoresistance [42].

1.4.3 Voltage-controlled storage memory

A new approach to energy-efficient data storage was offered by utilizing the strain induced phase transition in FeRh. This principle involves the integration of metamagnetic materials, such as FeRh alloys, with ferroelectric substrates, for example $BaTiO_3$ [43] or PMN–PT [24]. An applied electrical voltage deforms the ferroelectric crystal, thereby generating mechanical strain that is transferred to the FeRh layer. This leads to a shift in the T_t and can induce a phase change. While the change in magnetic moment can be utilized for spintronic applications [43], the accompanying giant electroresistance effect enables direct reading of information through a significant change in electrical resistance [24].

1.4.4 Requirements on thermal hysteresis

Within this chapter, we described the current understanding of the FeRh transition properties together with the remaining ambiguities. The applications discussed above, however, require further optimization of FeRh thin films and a deeper understanding of the mechanisms modifying the thermal hysteresis.

These applications impose requirements on all thermal hysteresis parameters, including the transition temperature T_t, the hysteresis width ΔT, and the residual magnetization M_res. In most applications, T_t should be very close to or slightly above room temperature in order to reduce or eliminate the need for external heating, which is often energy inefficient. The requirements for hysteresis width differ depending on the application. Thermoelectric sensors require a fast, linear response, which corresponds to a small hysteresis width. In contrast, for magnetic recording applications, a wide thermal hysteresis is beneficial because it provides a broader temperature interval of phase coexistence and may improve the thermal stability of the device. The promising concept of writing individual bits into phase domains creates a challenging requirement for the transition temperature range ideally between 270 K and 330 K.

Several mechanisms for tuning T_t have already been extensively studied, including strain, composition, doping, and irradiation. However, less attention has been given to controlling the width of the phase transition and the thermal hysteresis. As described in Section 1.1, these widths depend on activation energy barriers, defects, and layer

homogeneity. Therefore, the transition and hysteresis widths may vary with FeRh layer thickness [10], FeRh composition [29], or ion irradiation [6].
Finally, for the majority of applications, the residual magnetization should be minimized. It not only creates an unwanted background signal, but also reduces the fraction of the FeRh layer undergoing the transition. This becomes particularly critical in ultrathin FeRh films below 15 nm, where a significant portion of the measured magnetization can originate from residual ferromagnetic contributions. Residual magnetization therefore also limits the feasibility of preparing FeRh layers with thicknesses of only a few nanometers that still undergo a well-defined AF–FM phase transition.

2. Tunability upon deposition

The previous chapter discussed the main mechanisms controlling the thermal hysteresis characteristics of FeRh, including the transition temperature T_t, the hysteresis width ΔT and the residual magnetization M_{res} (defined in the section 1.1). The aim of this chapter is to investigate how these parameters can be tuned during sample preparation. Particular attention is paid to the influence of the substrate, FeRh thickness and sputtering pressure. The main objective is to identify deposition conditions that yield a phase transition close to room temperature, a broad thermal hysteresis, and a low residual magnetization.
The sample deposition and initial characterization by X-ray reflectivity (XRR), X-ray diffraction (XRD), and vibrating sample magnetometry (VSM) were performed by M.Sc. Jon Ander Arregi Uribeetxebarria, Ph.D within a broader research project. The analysis, comparison, and interpretation of the data together with the post-irradiation magnetic characterizations were carried out by the author within this thesis. The ion-beam measurements, ion irradiation and polarized neutron reflectometry (PNR) were carried out by the author together with the local team and equipment operators.

Table 2.1: Overview of FeRh samples and deposition parameters. The parameters varied for the optimization of the thermal hysteresis are highlighted.

Sample	Substrate	Ar pressure (10^{-3} mbar)	FeRh thickness (nm)	Pt thickness (nm)	Annealing (°C)	Time (min)
1	Al_2O_3	2.6	46	2	720	45
2	MgO	2.6				
3	Al_2O_3	2.6	28	2	720	35
4	MgO	2.6				
5	Al_2O_3	2.6	20	2	630	80
6	MgO	2.6				
7	MgO	2.6				
8	Al_2O_3	2.7	20	2	630	80
9	MgO	2.7				

The studied FeRh thin films (shown in the Table 2.1) were epitaxially grown on single-crystal MgO(001) and Al_2O_3(0001) substrates by magnetron sputtering from an equiatomic FeRh target on BESTEC Magnetron sputtering system. The nominal

FeRh thicknesses were 20, 28, and 46 nm. The FeRh growth was carried out at 360 °C under an Ar sputtering pressure of 2.6×10^{-3} mbar. For the second deposition batch of the 20-nm-thick films, a slightly higher Ar pressure of 2.7×10^{-3} mbar was used in order to test whether small changes in sputtering pressure, and therefore possibly in Fe/Rh composition, affect the transition parameters [29]. After deposition, the films were annealed to improve the chemical ordering of the B2 FeRh phase and were subsequently capped with a 2 nm Pt layer to prevent oxidation. The FeRh and Pt thicknesses determined by XRR agreed with the nominal values listed in Table 2.1 within approximately 1 nm. The roughness of the individual interfaces obtained from the XRR fits was below 0.5 nm. The only exception was sample 1 grown on Al_2O_3, whose surface showed visible damage after deposition. As a result, a reliable XRR fit could not be obtained for this sample. The XRR measurements were carried out at room temperature using a SmartLab Rigaku 9 kW diffractometer with monochromated Cu–Kα radiation ($\lambda = 1.5406$ Å).

Magnetic characterization was performed using a Quantum Design VersaLab VSM system. All samples exhibited the characteristic AF–FM transition. The magnetization curves shown in Fig. 2.1 were corrected for the temperature shift caused by the applied magnetic field, as well as for diamagnetic contributions from the substrate. The measured magnetic moment was converted to magnetization using the FeRh volume calculated from the nominal FeRh thickness and the sample area. This conversion assumes full coverage of the substrate by a homogeneous FeRh film. The measurements were performed in a constant magnetic field of 1 T. For sample 7, the accessible temperature range was insufficient to observe the complete transition at 1 T. Therefore, a magnetic field of 3 T was used in order to shift the transition to lower temperatures and observe a larger part of the phase transition.

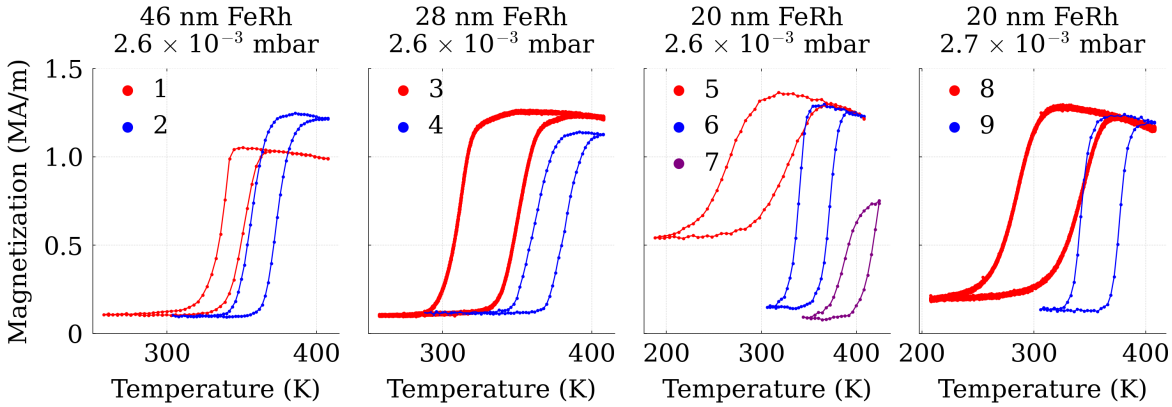


Figure 2.1: Temperature dependence of magnetization for the FeRh thin films listed in Table 2.1 measured by vibrating sample magnetometry (VSM).

The thermal hysteresis loops in Fig. 2.1 reveal pronounced differences not only in the T_t, but also in the ΔT, M_{res} and saturation magnetization. Part of these differences can be attributed to the controlled difference in substrates, FeRh thicknesses and Ar sputter pressure. However, unexpectedly large variations are also observed between samples prepared under nominally identical conditions. In particular, samples 6 and 7 were grown on the same substrate, with the same nominal thickness, Ar sputtering pressure,

and annealing conditions, yet their transition parameters differ significantly. This indicates that an additional, initially uncontrolled parameter affected the magnetic properties of the films.
A possible origin of these differences could be a variation in Fe/Rh composition or contamination by another element. Since FeRh is highly sensitive to stoichiometry and local disorder, even small compositional deviations could in principle lead to measurable changes in the T_t and hysteresis shape (Section 1.2.3). Therefore, ion-beam analysis using Rutherford backscattering spectrometry (RBS) and time-of-flight elastic recoil detection analysis (ToF-ERDA) was performed.

2.1 Chemical composition

Ion beam analysis was performed at the Tandem Laboratory at Uppsala University. RBS measurements were carried out using a 5 MV tandem accelerator by the author together with prof. André Vantomme. In the experiment, a 2 MeV He^+ beam was incident on the sample at an angle $\alpha = 7°$ with respect to the surface normal. The energy spectrum of the ions backscattered from the sample was measured using a detector with an energy resolution of 15 keV. The detector was positioned at an exit angle $\beta = 17°$, corresponding to a scattering angle $\theta = 170°$.

Table 2.2: FeRh and Pt layer parameters obtained from RBS analysis.

Sample	FeRh		Pt
	Areal density (10^{15} at./cm^2)	Fe concentration (at.%)	Areal density (10^{15} at./cm^2)
1	452	49.0 ± 1.3	12
2	338	48.1 ± 1.4	11
3	201	48.3 ± 1.7	11
4	208	49.8 ± 1.9	12
5	145	49.7 ± 0.5	11
6	148	49.3 ± 0.3	11
7	147	50.4 ± 1.2	11
8	145	49.6 ± 2.5	13
9	144	49.3 ± 2.3	12

Helium ions backscattered from light elements, such as O, Mg, or Al, lose a larger fraction of their energy, and therefore appear at lower energies in the detected spectrum. In contrast, ions backscattered from heavier elements, such as Pt, Rh, and Fe, retain more energy. Each element gives rise to a signal at a characteristic energy, forming elemental peaks in the RBS spectrum. The elemental composition can be determined from the integrated peak areas using the corresponding scattering cross sections. The peak width is affected by the detector resolution and by the thickness of the analyzed layer. Ions scattered from larger depths lose additional energy while travelling through

the material due to electronic stopping, which is described by the stopping power. As a result, peaks originating from thicker layers are broader, and their low-energy part corresponds to signals from larger depths, i.e., from the bottom part of the layer. This enables depth profiling of the layer composition [44].

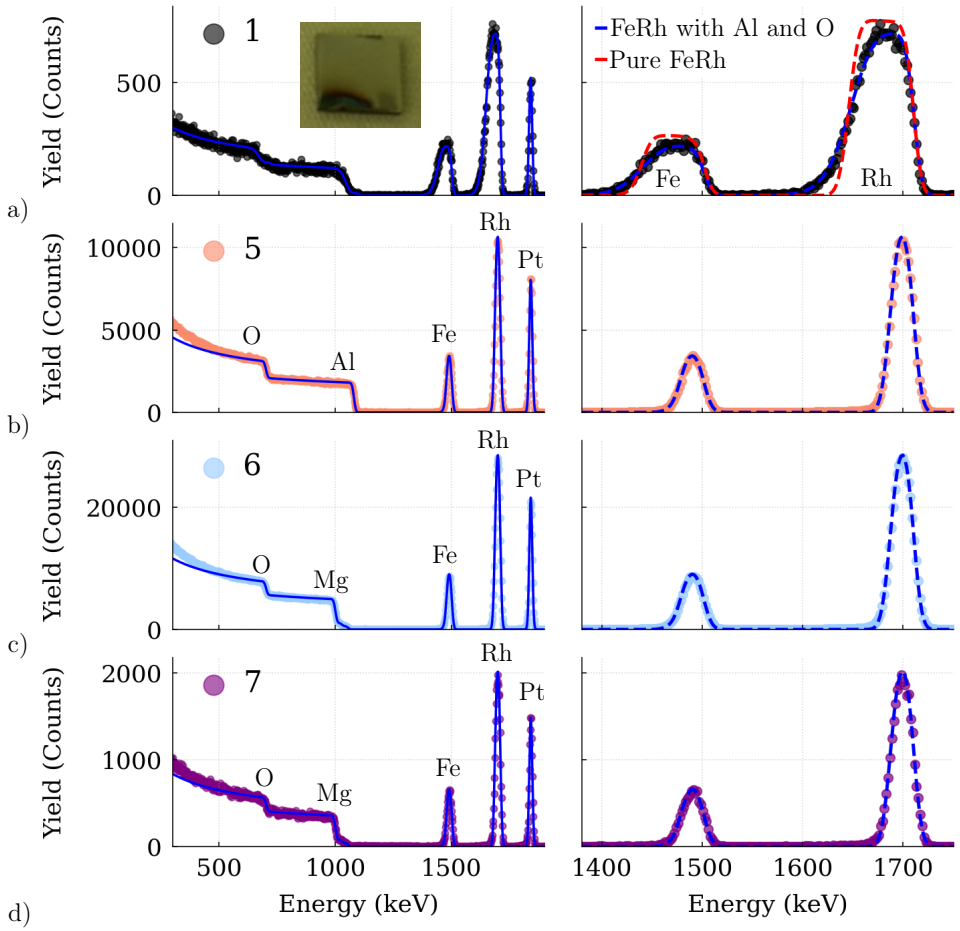


Figure 2.2: RBS spectra of samples 1, 5, 6, and 7. (a) RBS spectrum of sample 1. The right panel compares a fitting model with a pure FeRh layer to a model with a FeRh layer containing 14 at.% O and 6 at.% Al. Panels (b), (c), and (d) show the spectra of samples 5, 6, and 7, respectively, with well-defined elemental peaks and good agreement in corresponding fits.

Figure 2.2 shows the RBS energy spectra of samples 1, 5, 6, and 7 together with their fits obtained using the SIMNRA software [45] and the corresponding peak assignments. Sample 1 was visibly damaged in the region affected by the deposition clamps. Its previous XRR analysis also indicated increased roughness, which prevented reliable fitting. The RBS spectrum showed deformation of the Fe and Rh peaks, leading to deviations from the fit, as shown in Fig. 2.2. In order to obtain a satisfactory RBS fit for this sample, 14 at.% O and 6 at.% Al had to be included in the FeRh layer. This suggests only partial coverage of the substrate by the FeRh layer in the central region of the sample, where the ion beam was focused. Such discontinuous coverage could lead to an overestimation of the magnetic volume and, consequently, to an underestimation of the calculated magnetization. This could explain the reduced saturation magnetization

of sample 1 observed in Fig. 2.1.
The RBS spectra of samples 5, 6, and 7 exhibit narrower Fe and Rh peaks due to their smaller thickness. While sample 1 had a nominal thickness of 46 nm, samples 5, 6, and 7 were 20 nm thick. Their elemental peaks corresponding to the Pt capping layer and the FeRh film are well defined and show no visible deformation. Similarly smooth spectra with corresponding fits were observed for the other samples. The fit results are summarized in Table 2.1. The areal density describes the number of atoms within one column of unit area. Using the atomic mass and layer density, the areal density can be converted into a thickness. In particular, a 20 nm FeRh layer with a density of 9.9 g/cm^3 corresponds to an areal density of approximately 145×10^{15} at./cm^2, which is close to the FeRh areal density obtained for samples 5–9. This confirms the expected layer thickness.
The Fe concentrations c_{Fe} calculated from the Fe and Rh peak integrals are also listed in the Table 2.2. No systematic deviation in the Fe/Rh composition was found within the uncertainty intervals, which are given by the number of counts in the measured spectra. The average c_{Fe} obtained from RBS was 49.3 at.%, indicating that the films are slightly Rh-rich. As discussed in Section 1.2.3, a small Rh excess can stabilize the AF phase by reducing the probability of Fe antisite defects.

Table 2.3: Fe concentration of samples 5, 6, and 7.

Sample	Fe concentration (at.%)
5	49.7 ± 0.5
6	49.3 ± 0.3
7	49.8 ± 0.7

Because FeRh is highly sensitive to small compositional variations, additional RBS spectra were measured for samples 5, 6, and 7. The Fe concentrations obtained by combining the Fe and Rh peak integrals from all RBS measurements of the sample are summarized in Table 2.3. These values show only minor variations in c_{Fe} and overlap within their uncertainty intervals. Therefore, variations in the Fe/Rh stoichiometry are unlikely to be the dominant cause of the observed differences in the thermal hysteresis loops.
ToF-ERDA is an ion beam analysis technique used to determine the elemental composition as a function of depth. In contrast to RBS, ToF-ERDA is also sensitive to light elements [46], because it measures not only the kinetic energy of the recoiled atoms, but also their time of flight, which enables reliable mass separation of light elements and heavy elements even when they have small kinetic energies. In this experiment, a 36 MeV I^{8+} beam was used to elastically recoil atoms from the sample. The angle between the incoming beam and the sample surface was 22.5°, whereas the angle between the incoming beam and the detector was 45°. Both the time of flight and the kinetic energy of the recoiled atoms were measured, allowing the identification of

different elements according to their mass.

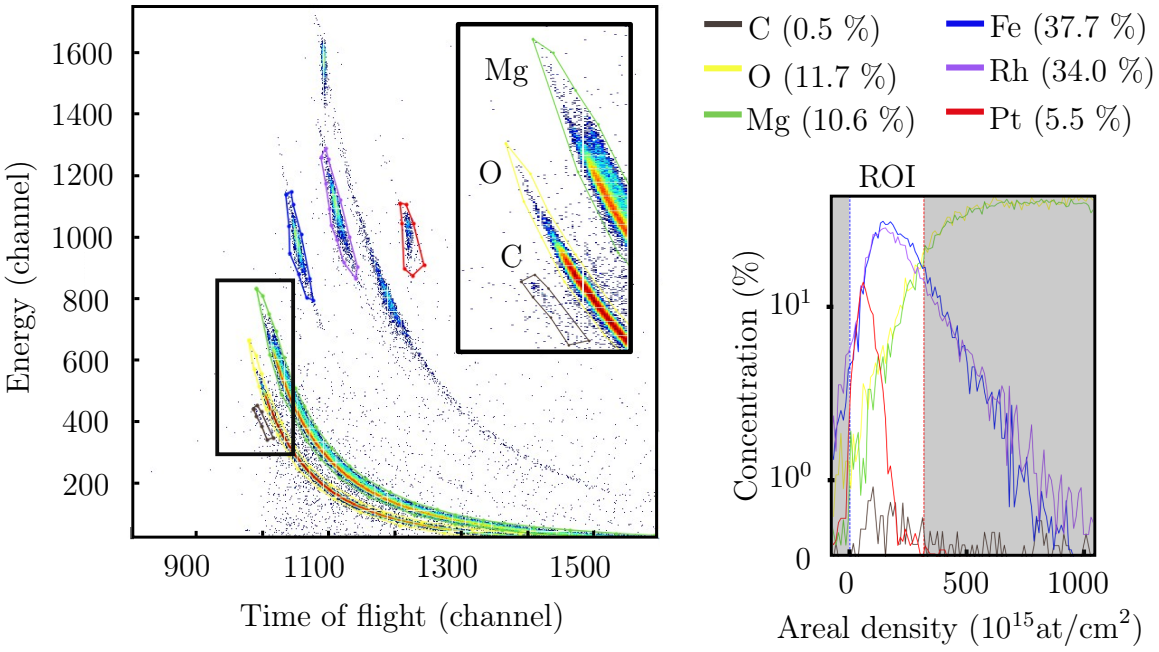


Figure 2.3: ToF-ERDA spectrum of sample 7 after surface cleaning in ethanol. The two-dimensional time-of-flight and energy spectrum shows traces corresponding to individual elements in the sample, together with one trace originating from the reflected iodine beam. The traces are outlined by the integration regions used to determine the elemental areal densities. The outline colors correspond to the elemental assignments shown in the legend. A weak additional trace attributed to carbon was observed. The evaluated concentration depth profile shown on the right, yields a carbon concentration of approximately 0.5 at.% within the marked region of interest. In ToF-ERDA depth profiles, the depth scale is commonly expressed as areal density, because the measured energy loss is directly related to the amount of material traversed by the recoiled atoms rather than to a geometric depth. The physical depth can be obtained by converting the areal density using the atomic density of the material. A zero areal density corresponds to the sample surface.

The distribution of detected ions depending on their time of flight and energy for sample 7 displayed in a Fig. 2.3. Each trace corresponds to atoms of a different element recoiled from the sample. The only trace without an elemental assignment originates from the scattered ion beam. By integrating an individual elemental trace, energy spectra similar to those obtained by RBS can be constructed and subsequently used for depth-profile reconstruction. Similarly to RBS, atoms recoiled from larger depths lose energy while travelling through the material, whereas atoms recoiled from the near-surface region retain higher energy. Therefore, the measured energy also contains information about the depth from which the atom originated. The depth-profile reconstruction was performed using the Potku software [47].
ToF-ERDA measurements were performed to exclude the possible influence of light-

element contamination in the studied samples. The analysis focused on samples 5 and 7. Both samples contained only a small amount of carbon, namely 0.6 at.% for sample 5 and 0.5 at.% for sample 7. Sample 7 was subsequently cleaned in ethanol and measured again in order to distinguish between surface contamination and carbon incorporated into the film. The carbon concentration remained 0.5 at.%, as shown in Fig. 2.3. A comparably low carbon content has previously been observed in FeRh samples [48]. At this concentration, carbon is not expected to account for the large differences in the thermal hysteresis observed here. Overall, the RBS and ToF-ERDA measurements confirm good layer purity and do not reveal any significant compositional differences that could account for the observed variation in thermal hysteresis.

2.2 Effect of substrate

The transition temperature in Fig. 2.1 is systematically lower for FeRh films grown on Al_2O_3 than for films grown on MgO under otherwise comparable deposition conditions. This indicates that the substrate plays an important role in controlling the phase transition.

The substrate influences the FeRh film mainly through epitaxial strain and quality of epitaxial growth. As discussed in Section 1.2, tensile strain facilitates the lattice expansion associated with the AF–FM transition and therefore stabilizes the FM phase, leading to a reduction of T_t. In contrast, compressive in-plane strain opposes the lattice expansion, stabilizes the AF phase, and shifts T_t to higher temperatures. For MgO, the nominal in-plane epitaxial strain is small and compressive, approximately $-0.3\,\%$. For Al_2O_3, the nominal epitaxial strain is much larger and tensile with values around 11.3% [8]. Such large nominal epitaxial strain is expected to be partially relaxed through defects and other strain relaxation mechanisms resulting in the actual strain state of the FeRh. The observed reduction of T_t for FeRh on Al_2O_3 is consistent with the expected effect of tensile strain. For sample pairs with the same nominal thickness and deposition conditions, the transition temperature is lower on Al_2O_3 than on MgO by approximately 23 K, 42 K, 60 K, and 48 K for samples (1,2), (3,4), (5,6), and (8,9), respectively (Fig 2.1). This trend is consistent with previous reports, where FeRh films grown on Al_2O_3 exhibited lower transition temperatures than comparable films grown on MgO [8, 25].

The substrate also affects the hysteresis width. In the present series, films grown on Al_2O_3 generally exhibit broader thermal hysteresis than films grown on MgO. The hysteresis broadening relative to the corresponding MgO samples is 20 K, 32 K, and 24 K for sample pairs (3,4), (5,6), and (8,9), respectively.

2.3 Effect of FeRh layer thickness

Film thickness is another important parameter that affects the transition temperature, hysteresis width, and residual magnetization. When the samples are grouped according to substrate, FeRh films grown on Al_2O_3 show a clear tendency: with decreasing

thickness, the transition temperature decreases, the thermal hysteresis broadens, and the residual magnetization increases (Fig 2.4a). This behavior can be qualitatively understood in terms of strain relaxation. In the thinnest films, the influence of the substrate is the strongest. For Al_2O_3, the tensile strain component stabilizes the FM phase and shifts the transition to lower temperatures. With increasing thickness, this strain is progressively relaxed, and the transition temperature tends to approach the bulk value of 350–360 K.

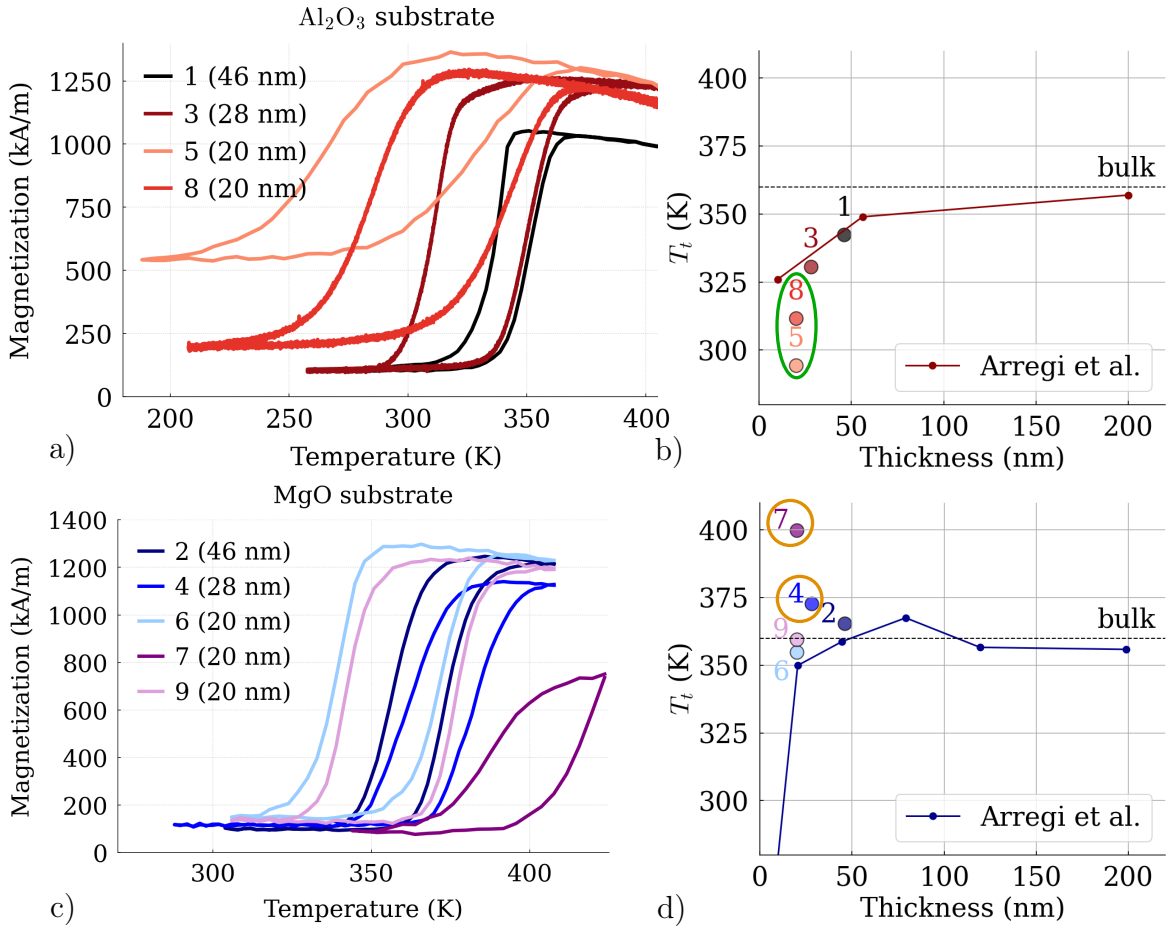


Figure 2.4: The figure shows a transition temperature as a function of FeRh thickness. Panels (a) and (c) show thermal hysteresis loops from samples grown on MgO and Al_2O_3 substrates, respectively, while panels (b) and (d) compare the corresponding thickness dependence of T_t with data adapted from Ref. [8]. Samples with the same nominal thickness but significantly different transition temperatures are highlighted in green, while samples deviating from the general trend are highlighted in orange.

An increase in M_{res} is observed for the 20-nm-thick samples grown on Al_2O_3. The increase in M_{res} for sample 8 is mild and at the edge of the uncertainty given by the volume evaluation. However, the M_{res} of sample 5 reaches 540 kA/m, corresponding to 40 % of its saturation magnetization. The origin of the large difference in M_{res} between samples 5 and 8 (that are marked green in the Fig 2.4b), reaching 360 kA/m, as well as their 18 K difference in T_t, remains unclear. Both samples have the same nominal thickness and substrate, and no significant compositional deviation of sample 5 was

detected by either RBS or ToF ERDA. It is also important to interpret the residual magnetization with caution when comparing samples with different FeRh thicknesses. As discussed in Section 1.1 the residual magnetization can originate from a ferromagnetic region at the FeRh/substrate interface, while an additional contribution may be distributed more uniformly throughout the FeRh layer. Since the magnetic parameters are evaluated from the magnetization, rather than directly from the total magnetic moment, the same interfacial FM layer can give rise to different apparent values of M_{res} depending on the total FeRh thickness. Consequently, the same interfacial FM contribution appears larger in thinner FeRh films, because it represents a larger fraction of the total FeRh volume. Therefore, an increased relative residual magnetization in thinner samples does not necessarily imply a larger absolute amount of ferromagnetic material.

For FeRh films grown on MgO, a simple strain based argument would predict the opposite trend from the FeRh films grown on Al_2O_3. Since MgO imposes a small compressive in-plane strain, the AF phase should be stabilized and the transition temperature should increase in thinner, more strongly strained films. However, the experimental behavior is more complex. In the present data, especially for the 20-nm-thick films, the transition temperature does not follow the trend expected solely from epitaxial strain. A comparison with previously published thickness dependent data is shown in Fig. 2.4d). The literature data also show that T_{t} decreases in sufficiently thin FeRh films and tends to converge toward the bulk value with increasing thickness [8] as observed for samples on Al_2O_3. The same trend in the T_{t}-on-thickness dependence for both MgO and Al_2O_3 suggests that the thickness dependence cannot be explained solely by the substrate induced strain, but there also has to be a significant impact of the thicknsess itself. Other previously reported thickness dependences for FeRh films on MgO also show a decrease of T_{t} with decreasing FeRh thickness, as summarized in Fig. 2.5 [49, 10].

A systematic separation of strain and finite thickness effects was reported in Ref. [10]. In the study, epitaxial FeRh films with thicknesses of 10, 15, 22, and 100 nm were grown on MgO, $KTaO_3$, and $SrTiO_3$ substrates. The authors showed that the transition temperature decreases significantly with decreasing thickness (Fig. 2.5). Below approximately 22 nm, the decrease becomes particularly pronounced, and for films thinner than 15 nm on MgO and $SrTiO_3$, T_{t} drops below room temperature. At the same time, the thermal hysteresis broadens systematically with decreasing thickness. The observed behavior was interpreted as a combined effect of epitaxial strain and film thickness. This was confirmed both experimentally and theoretically by density functional theory calculations. The finite thickness itself modifies the relative stability of the AF and FM phases, which results in a lower transition temperature. The broadening of the hysteresis in thin films was attributed to more difficult nucleation of both AF and FM domains, together with stronger pinning of domain walls [10].

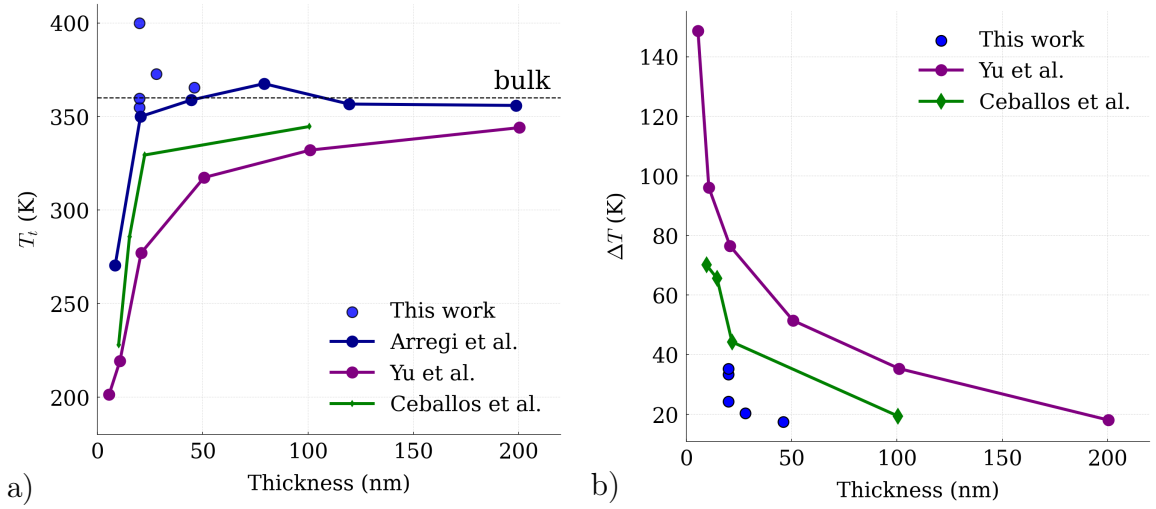


Figure 2.5: Thickness dependence of (a) the transition temperature T_t and (b) the hysteresis width ΔT. Selected data were adapted and modified from Refs. [49, 10, 8].

This could be also supported by difference in phase domains nucleation in 36-nm-thick and 200-nm-thick FeRh layers observed in thesis [33], where the 36-nm-thick layer exhibited broader thermal hysteresis with a lower transition temperature and significantly smaller phase domains. In contrast, the 200 nm layer exhibited narrow hysteresis, a high transition temperature, and phase domains hundreds of nanometers in size [33]. This may be related to the fact that in thin films, there is an increased concentration of defects due to the relaxation of epitaxial strain, which creates additional inhomogeneities and increases the diversity of nucleation sites. However, confirming this interpretation and identifying the microscopic mechanism responsible for the hysteresis broadening would require further investigation. These findings suggest that the anomalous behavior of the 20-nm-thick FeRh films on MgO substrates in the present series may be caused by a combination of finite thickness effects and an additional strain contribution that is not determined solely by the substrate material.

2.4 Additional source of strain

In the previous sections, the influence of chemical composition, substrate-induced epitaxial strain, and FeRh thickness was analyzed. Although these parameters explain the main trends in the thermal hysteresis behavior, the differences between samples 5 and 8 and between samples 6 and 7 remain unresolved. Therefore the XRD characterization was carried out to find the actual strain state of the film. The measurements confirmed high crystalline quality of the FeRh films. Small FCC FeRh peaks were observed for samples 1 and 3. Such peaks can occasionally appear during the growth of thicker FeRh films and are not expected to dominate the thermal hysteresis behavior. Therefore, the main analysis focused on the position of the FeRh(002) diffraction peak, which provides information about the out-of-plane lattice parameter c.
For samples grown on Al_2O_3, the interpretation of the room temperature lattice parameter is complicated by the fact that some samples are not fully in the AF state at

room temperature (Fig 2.4a). Since the FM phase has a larger lattice parameter than the AF phase, the measured value of c can contain contributions from both strain and the FM phase fraction. Therefore, the following discussion focuses mainly on samples grown on MgO, where all samples are predominantly AF at 300 K (Fig 2.4a).

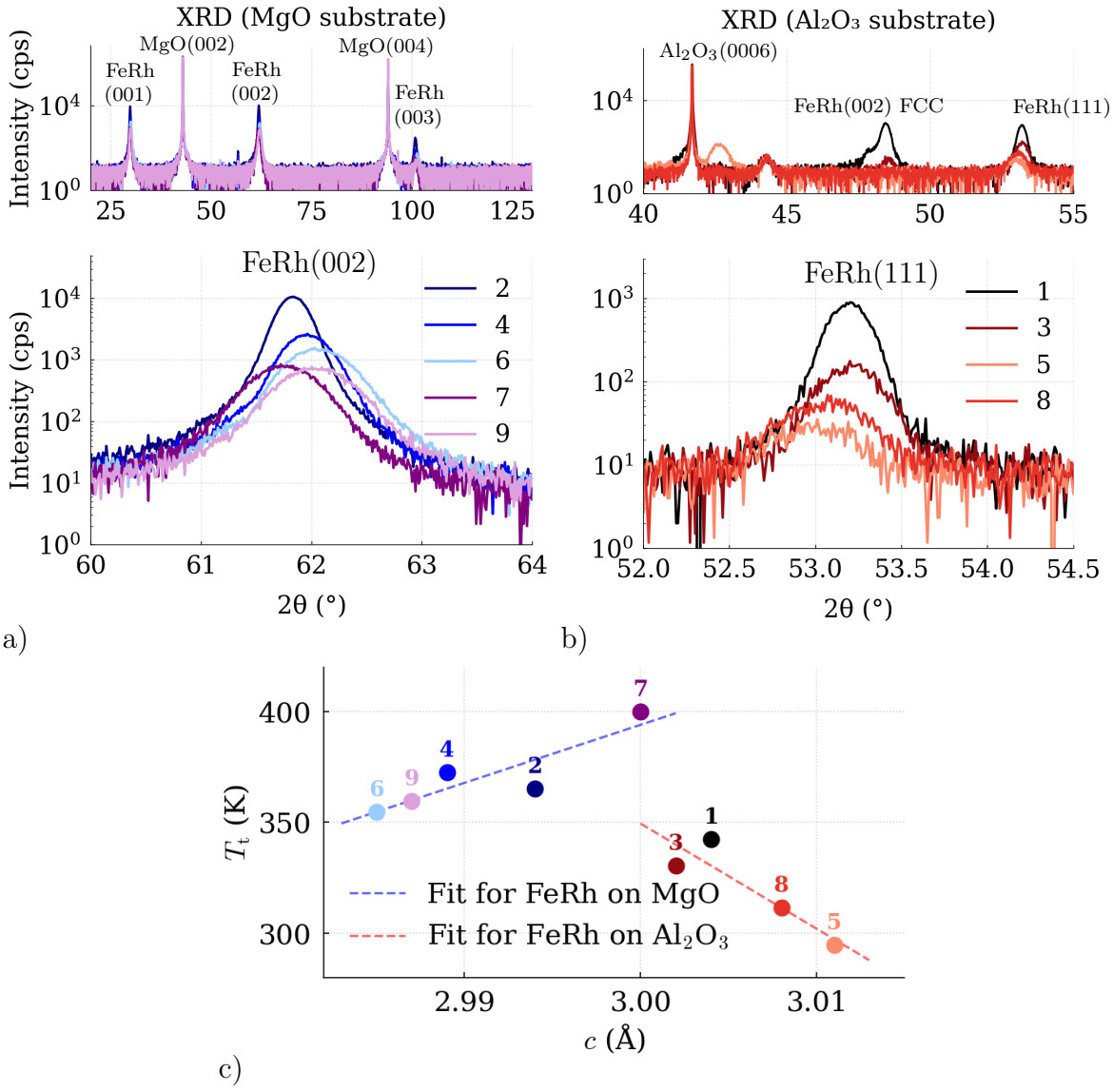


Figure 2.6: XRD analysis of FeRh films grown on (a) MgO and (b) Al_2O_3, together with the assignment of the main diffraction peaks. (c) Dependence of the transition temperature T_t on the out-of-plane lattice parameter c, with linear fits shown separately for each substrate.

The XRD measurements revealed a clear dependence of the FeRh(002) peak position on the magnetic transition temperature (Fig 2.6c). In particular, for the 20 nm FeRh films on MgO, where the nominal thickness contribution is identical, T_t depends linearly on the out-of-plane lattice parameter c. Such a dependence would be consistent with a scenario in which an increase in the out-of-plane lattice parameter c is caused by compression of the in-plane lattice parameter a (as is illustarted in the Fig 1.5 in the previous chapter). This suggests that an additional source of strain affected the c

together with the magnetic properties of the 20-nm-thick films.
A plausible origin of this strain is a mechanical clamping of the substrates during deposition. In the original deposition holder, the substrates were fixed at their edges using clamps tightened by screws. Variations in the tightening force could induce different strain states in the substrates and consequently in the growing FeRh layers. The clamping hypothesis was further supported by additional depositions performed with a modified sample holder (Fig 2.7a). In these depositions, new clamps with reduced mechanical contact were used for samples a, b, and c, whereas the original clamps were used for samples d, e, and f. The samples deposited with the new clamps showed much more reproducible thermal hysteresis loops and very similar transition temperatures (Fig 2.7b). In contrast, samples deposited with the original clamps again exhibited a larger spread in T_t. This comparison strongly suggests that the substrate mounting procedure can influence the strain state of the FeRh film and therefore its transition temperature.

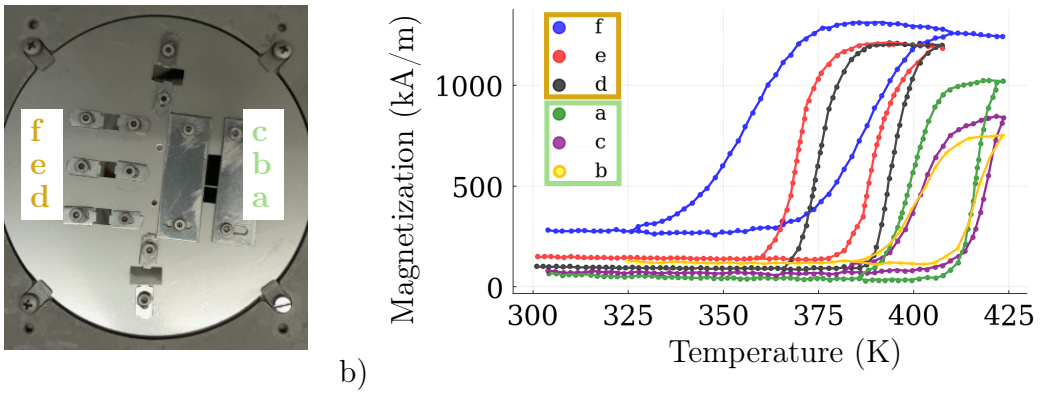


Figure 2.7: (a) Sample holder used during deposition, showing the original clamps on the left and the modified clamps on the right. (b) Thermal hysteresis loops of 30 nm FeRh films on MgO deposited with the modified clamps for samples a, b, and c, and with the original clamps for samples d, e, and f.

The linear dependence of T_t on strain is consistent with previous reports [25, 10]. However, when comparing films with different thicknesses, the finite thickness contribution must also be considered. As shown in Ref. [10], samples with different thicknesses can follow different dependencies of T_t on the tetragonal distortion c/a (Fig 2.8a). This means that the same value of strain does not necessarily produce the same transition temperature in films of different thicknesses. This picture is consistent with the present data. For 20-nm-thick FeRh films on MgO, T_t follows a linear dependence on the out-of-plane lattice parameter. A separate linear trend is observed for 30-nm-thick films. The 28-nm-thick sample lies between these two trends, as expected from its intermediate thickness. The main outliers are the 46-nm-thick sample 2 and 30-nm-thick sample f. The sample f was due to its deviation excluded from the linear fit of the 30 nm layers. Its lattice is much larger for its T_t, which could be related to the high residual magnetization (Fig 2.7b) that has a larger lattice parameter. These deviations might be caused by the fact that c does not directly describe strain. To further support the dependence of strain on T_t a direct measurement of the in-plane lattice parameter a,

for example by reciprocal space mapping, would be required.

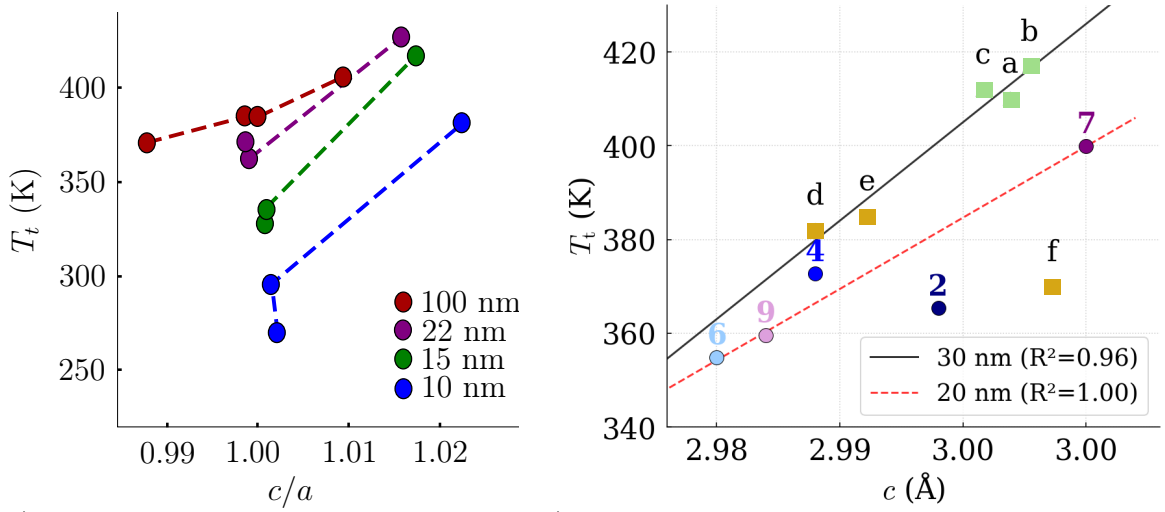


Figure 2.8: (a) Transition temperature T_t as a function of tetragonal distortion c/a, adapted from Ref. [10]. (b) Dependence of T_t on the out-of-plane lattice parameter for samples from the first and second deposition series.

2.5 Optimal deposition conditions

The results discussed above show that the thermal hysteresis of FeRh thin films can be significantly tuned by deposition parameters. The substrate has a strong influence on the transition temperature. Films grown on Al_2O_3 exhibit systematically lower T_t than films grown on MgO. This is consistent with the tensile strain component associated with Al_2O_3, which stabilizes the FM phase and shifts the transition to lower temperatures. At the same time, Al_2O_3 tends to broaden the thermal hysteresis.
Film thickness provides an additional tuning parameter. Reducing the FeRh thickness generally decreases the transition temperature and broadens the hysteresis. This trend cannot be explained by epitaxial strain alone and the finite thickness effect has to be considered.
The most suitable sample from the present deposition series is sample 8, consisting of 20-nm-thick FeRh grown on Al_2O_3 with an Ar sputtering pressure of 2.7×10^{-3} mbar. This sample exhibits a transition close to room temperature with $T_t = 312$ K, a thermal hysteresis width of 59 K, and a residual magnetization of 15 %.
The reproducibility of the transition parameters is strongly affected by the strain state of the film. The comparison of samples prepared with different substrate clamps indicates that even the mechanical mounting of the substrate during deposition can modify the FeRh lattice parameter and significantly impact the thermal hysteresis. Therefore, reliable tuning of FeRh upon deposition requires not only control of substrate and thickness, but also careful control of sample mounting and strain during growth.

3. FeRh ion irradiation

This chapter investigates ion irradiation as a post-growth method for tuning the thermal hysteresis of FeRh thin films. The irradiation experiments were performed at the Medium Energy Tandem Laboratory at Uppsala University using a high-current keV ion implanter. The investigated samples consisted of 28–30 nm FeRh layers grown by magnetron sputtering under the deposition conditions described in Chapter 2. The samples with their initial characterization were provided by M.Sc. Jon Ander Arregi Uribeetxebarria, Ph.D. and their post-irradiation magnetic characterizations were carried out by the author. The irradiations itself were performed by Mauricio A. Sortica, Ph.D. with the assistance of the author. Samples included both uncapped FeRh films and films capped with 2-nm-thick Pt layer. The Pt cap was used to protect the FeRh layer and prevent its oxidation. However, for irradiation experiments performed at elevated temperature, uncapped layers are preferred to avoid possible diffusion of the cap into the FeRh layer.

Previous studies have shown that ion irradiation can shift the FeRh transition temperature toward lower values, broaden the thermal hysteresis, and increase the residual magnetization [6, 50, 51]. These effects are generally attributed to irradiation-induced disorder. The irradiation may generate vacancies, interstitials, antisite-like disorder, and implanted ions. At sufficiently high fluence, the accumulated disorder can suppress the AF phase completely, leaving the film ferromagnetic over the entire temperature range. If the damage is increased further, degradation of crystallinity and a loss of the well-defined FeRh phase may occur, leaving the sample paramagnetic.

Irradiation can have multiple effects on the crystal structure, as it causes chemical disorder, doping, lattice vacancies, and also morphological defects or ion sputtering of the FeRh layer. The relative proportions of these effects can vary depending on the type of ion used, its energy, dose, or temperature during irradiation. The depth distribution of irradiation-induced defects can be estimated using SRIM simulations [52]. These simulations provide a useful comparison of ion ranges and vacancy profiles for different ion species and energies. Because SRIM does not include dynamic annealing, defect recombination, or temperature-dependent defect migration, the calculations indicate relative irradiation-induced damage rather than exact concentrations of stable defects. Figure 3.1 illustrates two important trends. First, increasing the ion energy shifts both the ion range and the vacancy maximum deeper into the sample. Second, lighter ions have a smaller scattering cross section and therefore penetrate deeper while producing fewer displacements per incident ion. Heavy ions, in contrast, produce stronger near-surface damage and are more likely to generate dense collision cascades.

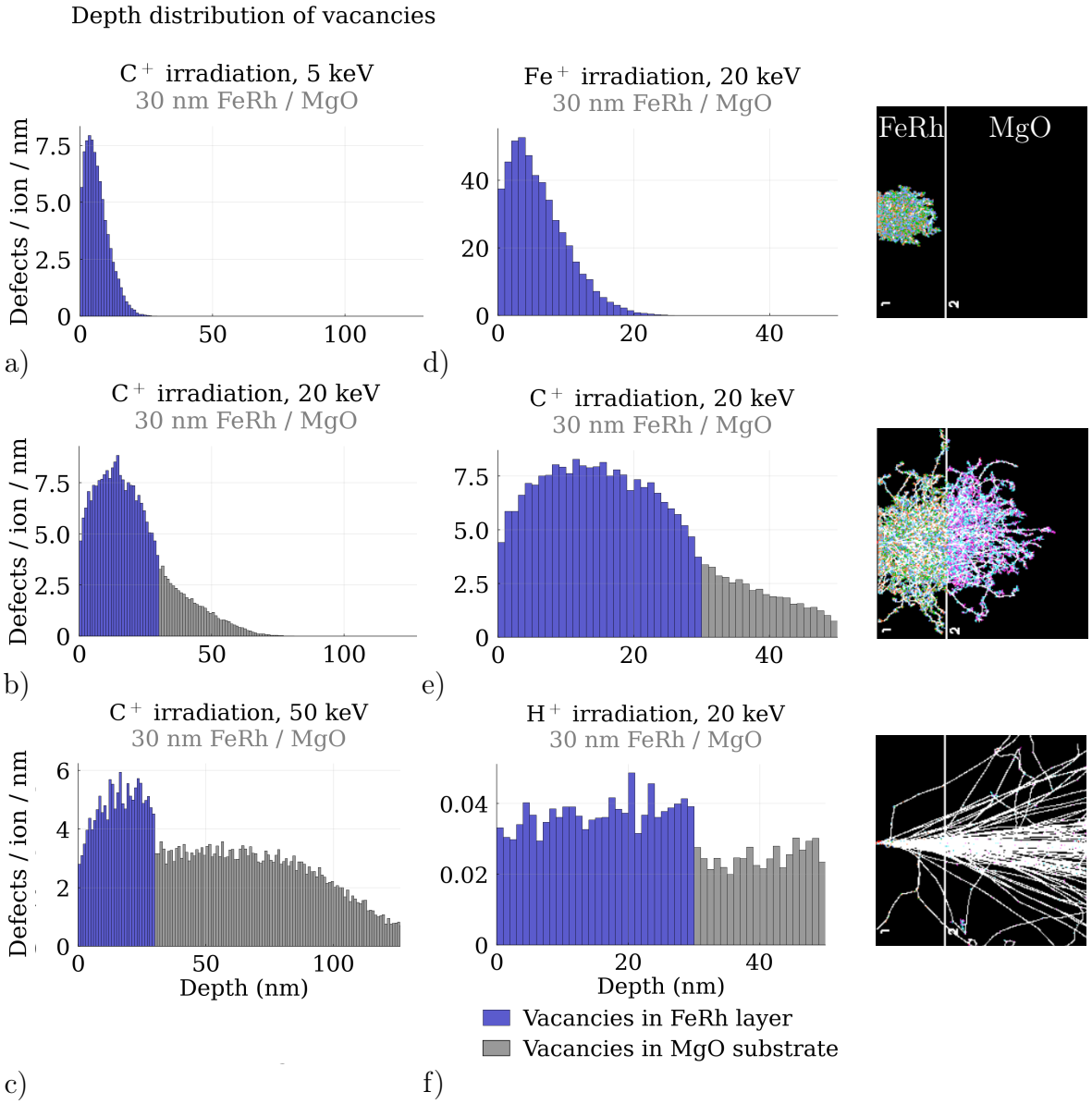


Figure 3.1: SRIM simulations of irradiation-induced vacancy profiles and ion ranges in a 30-nm-thick FeRh layer on MgO. Panels (a)–(c) compare C^+ irradiation at different ion energies, showing the increasing penetration depth with increasing energy. Panels (d)–(f) compare 20 keV irradiation by ions with different masses. Heavy ions such as Fe generate a much larger number of near-surface vacancies and are stopped within the FeRh layer, whereas light ions such as H penetrate deeper and generate fewer vacancies.

The SRIM simulation in Fig. 3.2a shows that the concentration of vacancies exceeds the concentration of the implanted ions by several orders of magnitude. This suggests that the dominant effect of irradiation is not chemical doping, but rather irradiation-induced modification of the crystal structure. A similar conclusion can be drawn from previous irradiation studies. In Ref. [51], the number of generated defects was reduced by using very light ions with an energy of only 3.8 keV. In addition, a 15-nm-thick Ag capping layer was deposited to protect the FeRh film. Such conditions, according to SRIM simulations, create a system where the doping is maximized relative to induced defects. However, even in such a system, according to the [51], the concentration

of Fe/Rh displacements is 10–50 times higher than the concentration of implanted He. Therefore, He alone as a chemical dopant is probably not the main cause of the observed changes. The observed changes are attributed mainly to irradiation-induced disorder, including vacancies, interstitials, and Frenkel-pair-like defects, rather than to a simple chemical doping effect.
In contrast, Ref. [6] used a different strategy based on 25 keV Ne^{5+} irradiation. In this case, a comparable modification of the magnetic transition was achieved at much lower fluences, because the heavier ions produced a higher density of lattice displacements. In the case of five-times ionized neon, the doping is negligible, since the majority of the ions pass through the FeRh layer. Despite these different irradiation conditions, both studies reported the same qualitative trend: with increasing irradiation fluence, the transition temperature T_t decreased, the thermal hysteresis broadened, and the residual ferromagnetic magnetization M_{res} increased [6, 51]. This again indicates that the modification of the FeRh phase transition is primarily governed by irradiation-induced lattice disorder. For hydrogen irradiation, which led to a similar phenomenology, namely an increase of the M_{res} and a decrease of T_t with increasing irradiation dose, structural and chemical analyses supported by first-principles calculations suggest that local structural distortions and Fe–Frenkel defect formation weaken Fe–Rh hybridization and thereby stabilize the FM state [50].
The main irradiation experiments, conducted within this work, focused on 20 keV C^+ and H^+ ions. Carbon was selected for several reasons. First, based on the SRIM calculations, its mass provides a broad vacancy profile across a 30-nm-thick FeRh layer. Second, according to the ternary alloy considerations based on valence electron concentration, carbon incorporation is expected to decrease the transition temperature T_t [5]. Third, ToF-ERDA measurements revealed that a small amount of carbon is already present in the FeRh layers, as discussed in Section 1.2.3, which reduces the additional chemical complexity introduced by ion implantation. C^+ irradiation has not, to the best of our knowledge, been systematically studied in FeRh. Another chosen element was hydrogen, which, on the other hand, was previously reported to induce Fe–Frenkel defects in FeRh [50]. Due to its small mass, a large fraction of 20 keV H^+ ions penetrates through the FeRh layer and reaches the substrate, inducing point-like defects. H^+ could offer a more uniform vacancy distribution reaching the FeRh/MgO interface. This makes H^+ irradiation particularly relevant for modifying the interfacial residual ferromagnetic contribution.

3.1 C^+ irradiation

The first C^+ irradiation experiment was performed on a 30-nm-thick FeRh film grown on MgO without a capping layer with fluences 1.7×10^{13} cm^{-2} and 5×10^{13} cm^{-2}. As shown in Fig. 3.2, irradiation produced the same qualitative trend as previously reported for Ne and He irradiation. The transition temperature decreased, while the hysteresis width and residual magnetization increased [6, 51]. The fluence of 5×10^{13} cm^{-2} suppressed the AF–FM transition within the measured temperature range,

leaving the sample predominantly ferromagnetic.

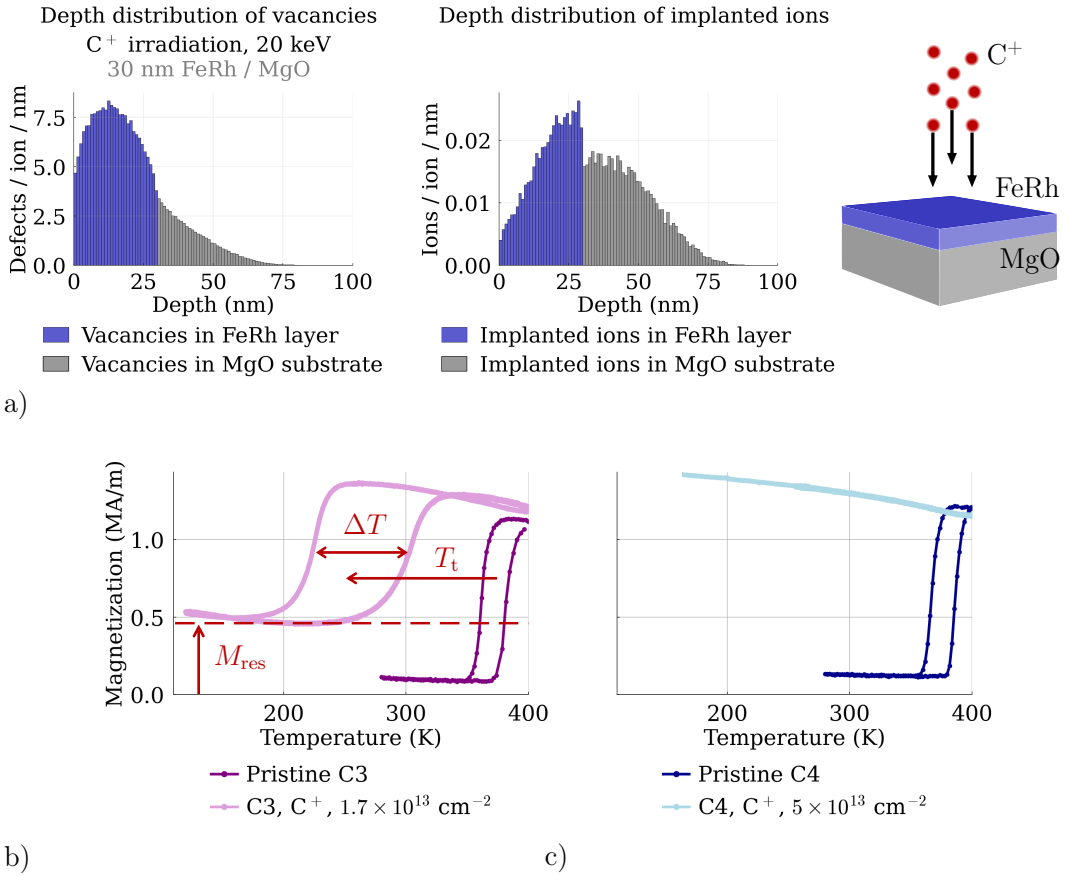


Figure 3.2: Initial 20 keV C^+ irradiation of a 30-nm-thick FeRh layer on MgO substrate. (a) SRIM vacancy profile and ion range for 20 keV C^+ irradiation. The vacancy production is much larger than the concentration of implanted carbon ions. (b) Modification of the thermal hysteresis after irradiation with a fluence of 1.7×10^{13} cm^{-2}. (c) Irradiation with 5×10^{13} cm^{-2} suppresses the AF–FM transition within the measured temperature range.

Before performing a systematic dose dependence, the reproducibility of the irradiation response was tested using two FeRh films with different initial transition temperatures. Both samples were 30-nm-thick FeRh films grown on MgO without a capping layer and originated from the same deposition batch. Their initial transition temperatures were 372 K and 414 K. As discussed in Section 2.4, such differences between nominally similar samples are most likely related to different strain states, possibly caused by substrate clamping during deposition. Both samples were irradiated with 20 keV C^+ ions at a fluence of 1.7×10^{14} cm^{-2}. The relative shifts of the heating and cooling branches are shown in Fig. 3.3. The irradiation shifted both hysteresis loops to lower temperatures, but the magnitude of the shift depended on the initial state of the sample. The shift of the heating branch was similar for both samples, whereas the shift of the cooling branch was significantly larger for the sample with the lower initial T_t. As a consequence, this sample exhibited a much stronger hysteresis broadening after irradiation.

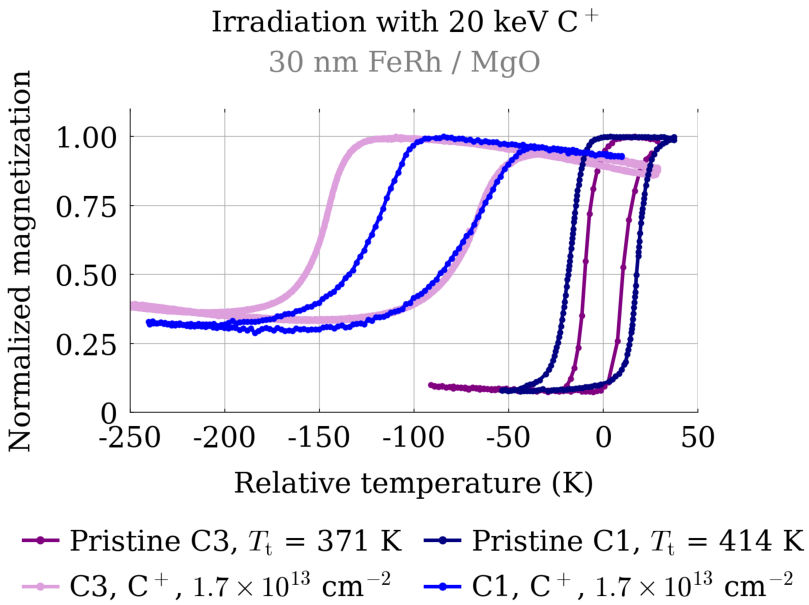


Figure 3.3: Relative shift of the thermal hysteresis after 20 keV C^+ irradiation of two 30-nm-thick FeRh films grown on MgO with different initial transition temperatures. The sample with the initial transition temperature $T_t = 414$ K shows a shift of 80 K on the heating branch, a shift of 100 K on the cooling branch, and an increase in the hysteresis width ΔT by 10 K. The sample with the initial transition temperature $T_t = 371$ K shows a shift of 80 K on the heating branch, a shift of 140 K on the cooling branch, and an increase in ΔT by 60 K.

This result shows that the irradiation response cannot be evaluated independently of the initial strain state. Direct comparison of fluence-dependent irradiation effects therefore requires samples with the same initial properties. For this reason, dose-dependent experiments were performed on pieces cleaved by sharp tip from the same original film, so that different irradiation conditions could be applied to nominally identical layers.

3.1.1 Dose dependence

A more systematic dose-dependent study was performed on a 28-nm-thick FeRh layer grown on Al_2O_3 and capped with 2-nm-thick Pt layer. The sample was cleaved into several pieces, allowing different fluences to be applied to parts of the same original film. The dose dependence is shown in Fig. 3.4. Increasing the C^+ fluence gradually shifts the hysteresis toward lower temperatures, broadens the transition, and increases the residual magnetization. The largest hysteresis width reached 84 K. This broadening was accompanied by an increase of M_{res} by about 30% and by a reduction of T_t by 111 K, down to 227 K. The saturation magnetization also changed with fluence, but these changes remained within the estimated experimental uncertainty of approximately 10–20%, which is dominated by the uncertainty in the FeRh volume estimation of the irregularly cleaved samples.
The irradiated samples were subsequently annealed in vacuum at 470 K for 30 min. Annealing partially reversed the irradiation-induced changes. The thermal hysteresis

shifted back toward the pristine state, the residual magnetization decreased, and the transition became sharper. This indicates partial recovery of the irradiation-damaged lattice.

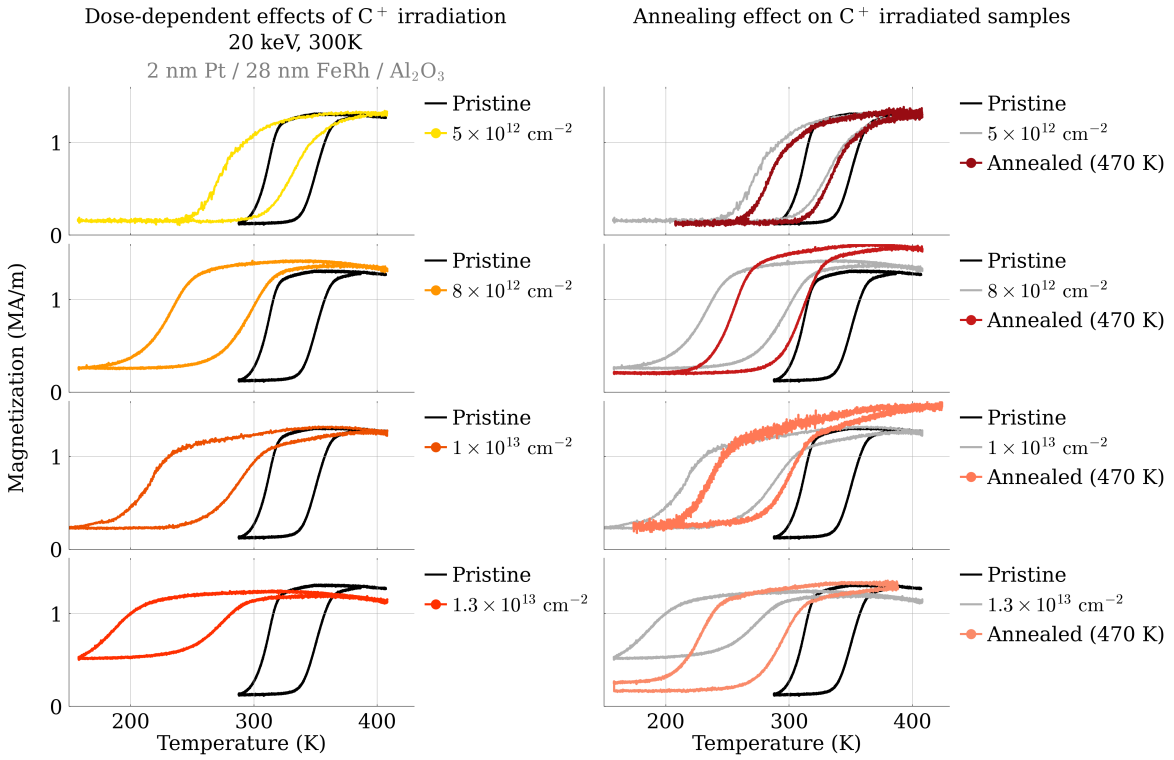


Figure 3.4: Dose dependence of 20 keV C^+ irradiation in a 28 nm $FeRh/Al_2O_3$ film capped with 2 nm Pt. The left panel shows the gradual shift and broadening of the thermal hysteresis with increasing fluence. The right panel shows the partial recovery of the hysteresis after subsequent annealing.

3.1.2 Irradiation at elevated temperature

Another strategy for controlling irradiation-induced defects is to irradiate the sample at elevated temperature. In this case, defect formation and defect recovery occur simultaneously. The corresponding results are shown in Fig. 3.5. Compared with room-temperature irradiation, elevated-temperature irradiation reduced the downward shift of T_t and suppressed the increase in residual magnetization, while a broadened hysteresis remained prominently preserved. For irradiation at 200 °C, the resulting hysteresis was centered near 314 K and had a width of 51 K.

A small secondary hysteresis loop was observed after elevated-temperature irradiation at 470 K, as is highlighted with green mark in Fig. 3.5a. Changes in optical reflectivity revealed a distinct region at the sample edge that transitioned at higher temperature and corresponded to the temperature range of the secondary loop. This feature is attributed to a part of the sample that was partially shadowed by the clamp during irradiation. Since this region received a reduced irradiation fluence, its transition temperature remained higher and closer to that of the pristine sample.

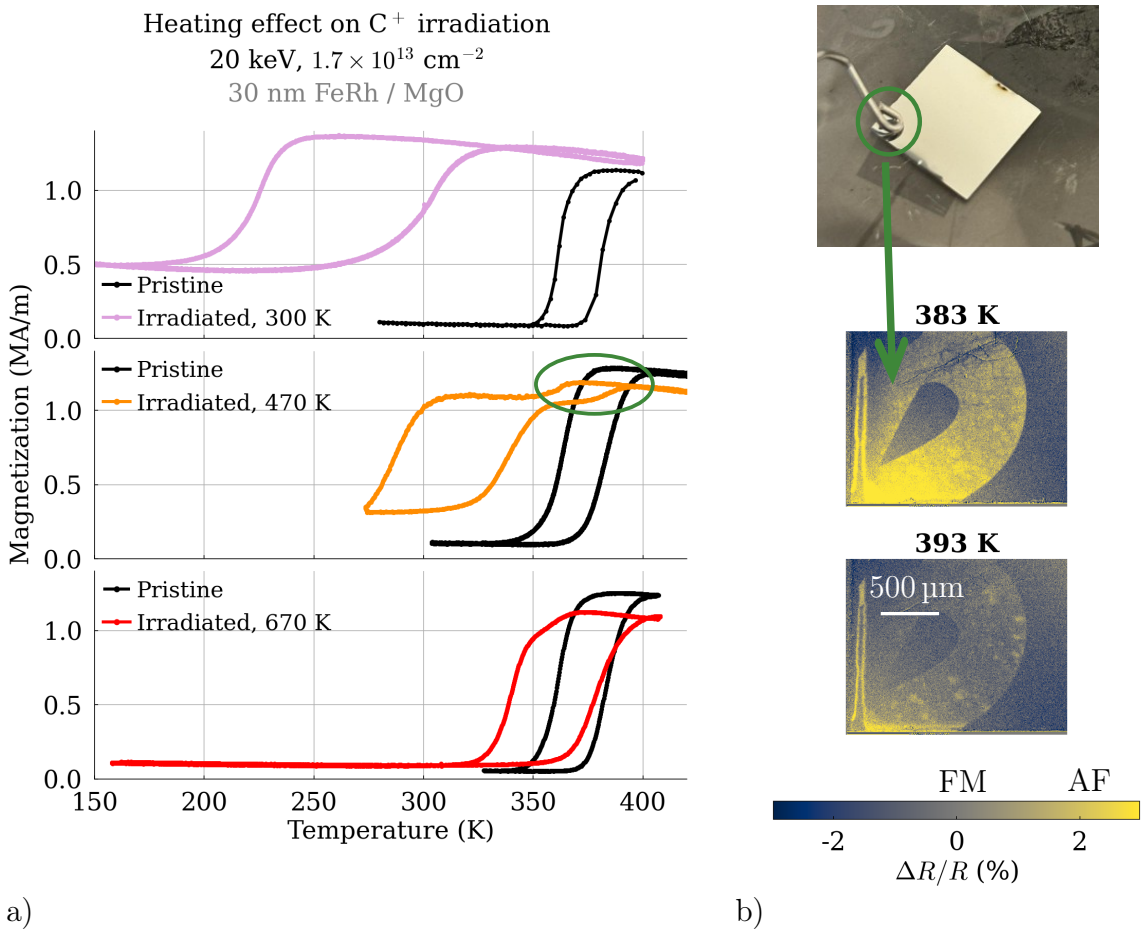


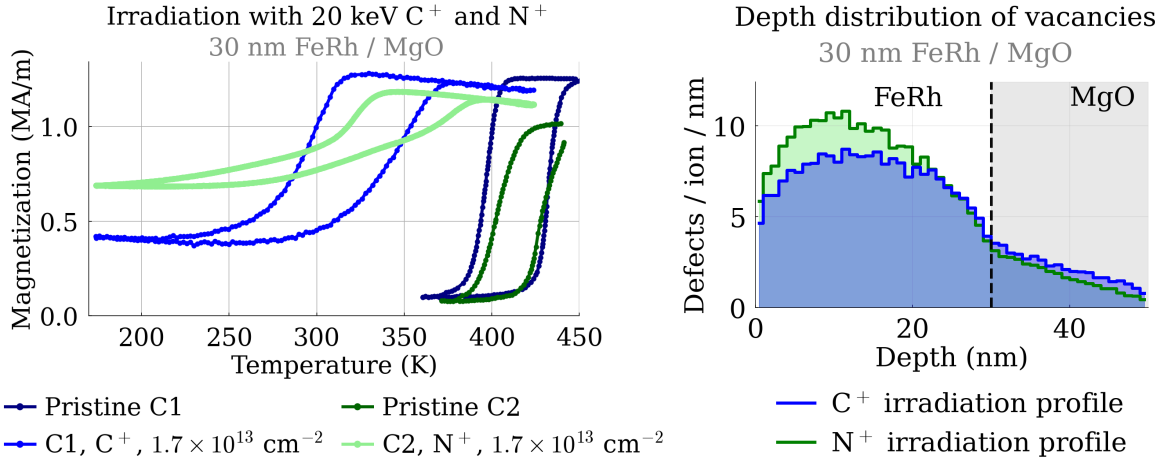
Figure 3.5: Effect of elevated temperature during 20 keV C^+ irradiation. (a) Thermal hysteresis after irradiation at different temperatures. Elevated-temperature irradiation reduces the magnitude of the irradiation-induced shift. A secondary minor loop is attributed to partial shadowing by the sample clamp. (b) The map of changes in optical reflectivity showing the clamp-shadow region responsible for the secondary thermal hysteresis loop visible in the sample irradiated at 470 K (green mark). The reflectivity image was obtained by substraction of an image at 400 K with sample in the fully FM phase, thus zero corresponds to the FM phase and its change to areas in AF phase.

3.2 C^+ and N^+ irradiation

The effects of C^+ and N^+ irradiation were compared using identical irradiation parameters. Two samples with similar initial thermal hysteresis and relatively high transition temperatures were selected. The resulting thermal hysteresis loops and corresponding SRIM vacancy profiles are shown in Fig. 3.6.

Both ion species shifted the transition toward lower temperature and increased the residual magnetization. However, the N^+-irradiated sample exhibited a more distorted hysteresis shape and a larger residual ferromagnetic contribution. The transition temperatures after irradiation were similar, with $T_t \approx 316$ K for the C^+-irradiated sample and $T_t \approx 315$ K for the N^+-irradiated sample. The residual magnetization, however, increased to 30% for C^+ irradiation and to 40% for N^+ irradiation.

This difference can be qualitatively explained by the different vacancy depth profiles. Both profiles exhibit a vacancy maximum near the surface and a gradual decrease toward the FeRh/MgO interface. However, the N^+ profile is less uniform and has higher concentration of vacancies near the surface. The maximum in the vacancy depth profile increases from approximately 8 vacancies per ion per nm for C^+ to approximately 10 vacancies per ion per nm for N^+, corresponding to an increase of about 20%. Such increase in inhomogeneous defect distribution may divide the film into regions with different local transition temperatures: a strongly damaged near-surface region with enhanced FM stability and a deeper, less damaged part that retains a more pronounced transition. This can explain the stronger deformation of the hysteresis loop and the higher residual magnetization after N^+ irradiation.



a) b)

Figure 3.6: Comparison of 20 keV C^+ and N^+ irradiation. (a) Thermal hysteresis after irradiation. The C^+-irradiated sample has $T_t = 316$ K, $\Delta T = 51$ K, and $M_{res} = 30\%$. The N^+-irradiated sample has $T_t = 315$ K, $\Delta T = 45$ K, and $M_{res} = 40\%$. (b) SRIM vacancy depth profiles showing a larger and more surface-weighted amount of vacancies for N^+ irradiation.

3.3 H^+ irradiation

To investigate the effect of H^+ irradiation, 30-nm-thick FeRh film grown on MgO without a capping layer was used. The pristine film exhibited transition temperatures between approximately 370 and 430 K. Such high transition temperatures introduced an experimental limitation, since the accessible temperature range of the VSM did not allow the complete thermal hysteresis loop to be measured. As a result, only minor loops were measured.

Compared with C^+ irradiation, substantially higher H^+ fluences were required to produce a measurable modification of the phase transition. This is expected because hydrogen is much lighter and has a smaller scattering cross section, resulting in fewer collision events and a lower density of lattice displacements within the FeRh layer. No clear change in the T_t or hysteresis shape was observed for fluences on the order

of 1×10^{13} cm^{-2}, which were already sufficient to modify the transition in the case of C^+ irradiation. In contrast, the effects of H^+ irradiation became visible for fluences of 5×10^{14} and 1×10^{15} cm^{-2}. The Fig. 3.7a shows modification of the thermal hysteresis of sample H1, that was cleaved into 2 parts. Each part was afterwards irradiated with one of the aformentioned fluences. The H^+ irradiation again shifted the thermal hysteresis toward lower temperatures and increased residual magnetization, which is a similar to tendency reported for hydrogen-irradiated FeRh films, where increasing H^+ dose enhanced the residual ferromagnetic state and reduced the transition temperature [50] inducing Fe-Frenkel defects.
After irradiation, the sample exposed to a fluence of 5×10^{14} cm^{-2} was annealed at 470 K. Annealing partially reduced the irradiation-induced modification and shifted the transition back toward that of the pristine sample, as was observed after annealing of C^+-irradiated samples. This again indicates that part of the irradiation-induced disorder is reversible at elevated temperature.

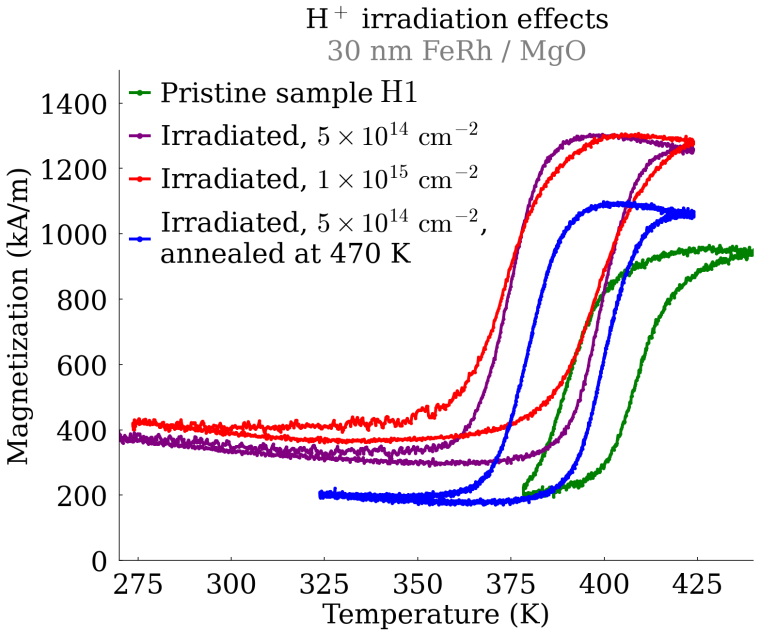


Figure 3.7: Effect of H^+ irradiation on a 30-nm-thick FeRh films grown on MgO. Temperature dependence of magnetization for the pristine and irradiated samples. The pristine film was cleaved into two pieces, which were irradiated with fluences of 5×10^{14} and 1×10^{15} cm^{-2}. The sample irradiated with 5×10^{14} cm^{-2} was subsequently annealed at 470 K.

3.4 Localization of the residual magnetization

After deposition, FeRh thin films exhibit a finite residual magnetization M_{res} in the nominally AF state that usually reaches values of approximately 5–15%, depending on the layer thickness. After ion irradiation, M_{res} increases. The magnitude of the increase depends on the ion species, fluence, and irradiation conditions. The purpose of this section is to examine whether the residual FM contribution is localized laterally,

for example near damaged regions, or across the film thickness, for example near the substrate interface or close to the film surface.
The lateral distribution of the residual magnetization was first investigated by optical microscopy at room temperature. A background image was acquired and subtracted from images recorded during a magnetic-field sweep from −200 to 200 mT at 300 K. Since the samples are predominantly in the AF state at this temperature, field-dependent changes in the optical reflectivity are attributed to regions with a residual FM contribution. In some samples, a field-dependent signal was observed mainly close to the sample edges. For example, in a cleaved sample irradiated with 20 keV H^+ ions at a fluence of 5×10^{14} cm^{-2}, the magnetic response was most pronounced near the cleaved edge and close to the regions affected by deposition clamps, as shown in Fig. 3.8. These regions may be influenced by local strain, imperfect film continuity, contamination, or temperature gradients during deposition. Such local perturbations can stabilize small FM regions even when the majority of the film remains AF. Away from the sample edges and visibly damaged areas, no pronounced lateral variations were observed. However, local Kerr measurements still showed ferromagnetic hysteresis, indicating rather laterally homogeneous residual FM contribution. MFM measurements performed in the AF state also did not reveal clear lateral magnetic inhomogeneities across the central part of the layer.

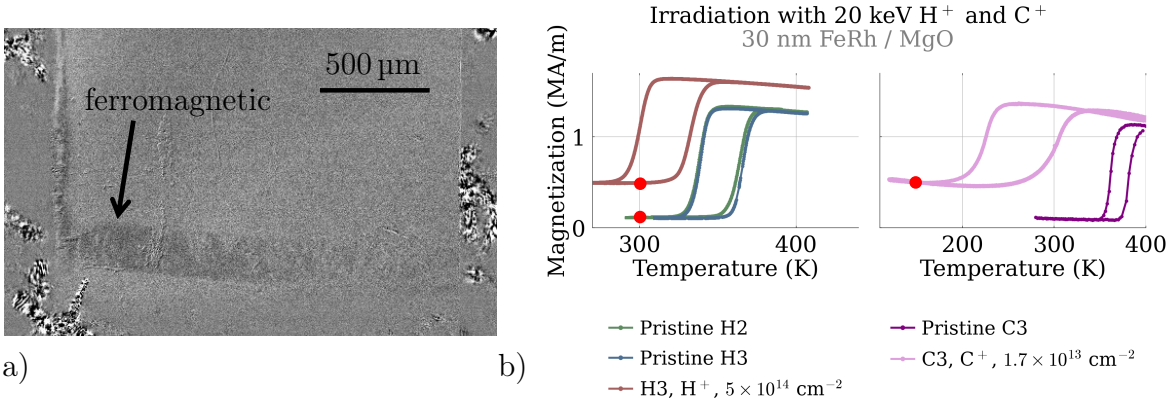


Figure 3.8: (a) Change in optical reflectivity during a magnetic-field sweep from −200 to 200 mT. A field-dependent response is observed mainly at the sample edges, especially near the deposition clamps and at the cleaved edge. (b) Thermal hysteresis of 30-nm-thick FeRh films grown on MgO. The left panel shows two as-grown samples, H2 and H3, with similar thermal hysteresis. The thermal hysteresis of sample H3 is also shown after 20 keV H^+ irradiation at a fluence of 5×10^{14} cm^{-2}. The right panel shows sample C3 before and after 20 keV C^+ irradiation. The red points indicate the temperatures at which polarized neutron reflectometry measurements were performed.

To obtain information about the vertical distribution of the residual magnetization, polarized neutron reflectometry (PNR) was performed at the SuperADAM reflectometer. The instrument uses a monochromatic neutron beam with a wavelength of 5.21 Å, polarization optics, and a two-dimensional position-sensitive detector [53]. PNR measures spin-dependent reflectivity curves and allows the reconstruction of depth-dependent nuclear and magnetic scattering length density (SLD) profiles [54].

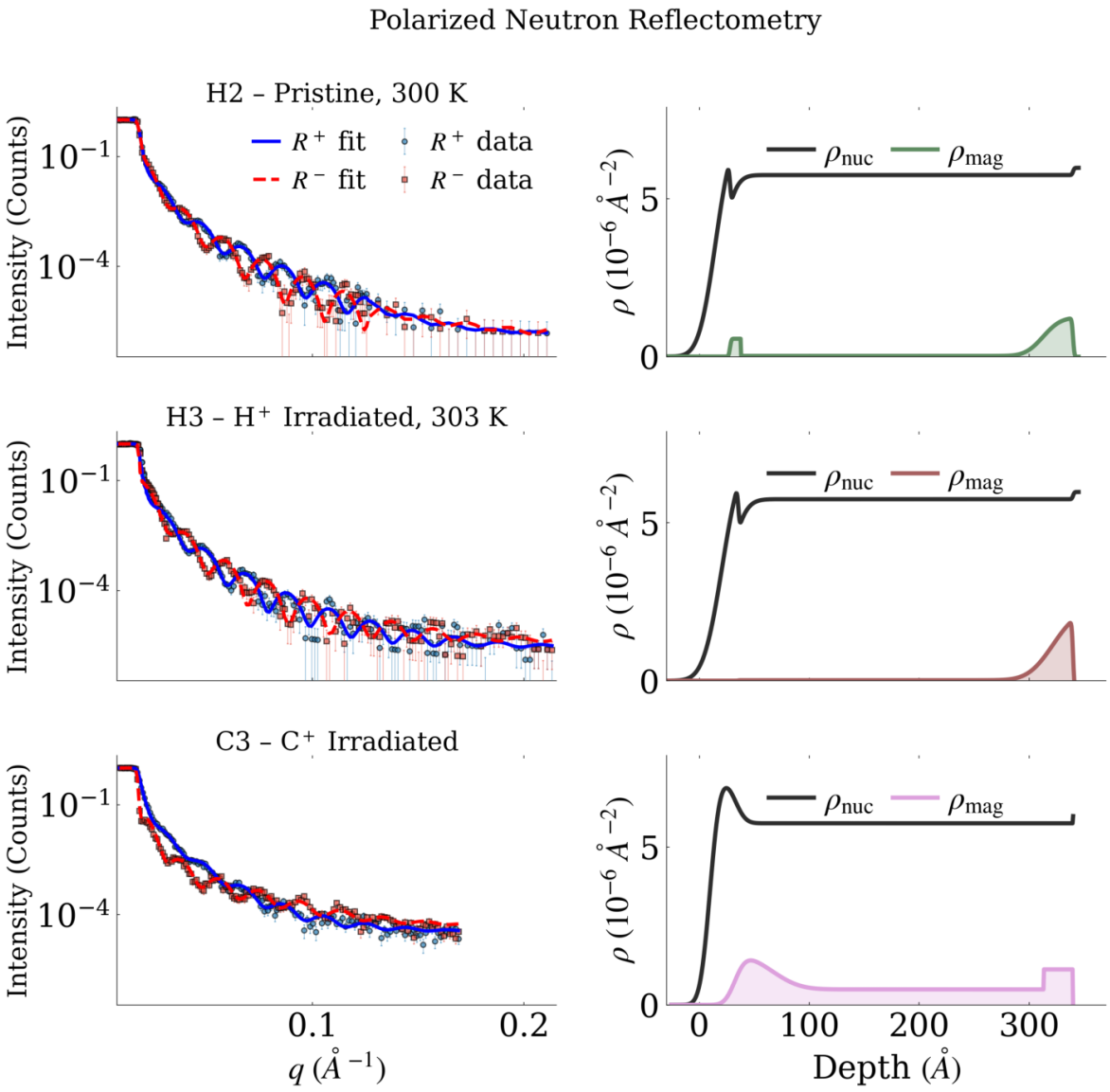


Figure 3.9: Polarized neutron reflectometry results for pristine, H^+-irradiated, and C^+-irradiated FeRh layers. The left column shows the measured spin-up and spin-down reflectivity curves, R^+ and R^-, together with the corresponding fits. The figures of merit describing the fit quality are 0.092, 0.114, and 0.078, respectively. The right column shows the nuclear scattering length density ρ_{nuc} and magnetic scattering length density ρ_{mag} depth profiles obtained from the fits.

Spin-up and spin-down reflectivity spectra were measured in an in-plane external magnetic field of 500 mT at selected temperatures. The fitting was performed using the GenX software [55]. To obtain a reliable simulation, three fitting procedures were applied for each sample. The first model consisted of a single FeRh layer. In the second model, the FeRh layer was divided into three sublayers with similar FeRh density, while the magnetic moment and thickness were fitted for each sublayer. The third model was the most complex and consisted of ten sublayers with fixed thicknesses. The magnetic moment of each sublayer was fitted together with one common thickness parameter. These models were then compared to verify that they followed similar trends. The final depth profile was chosen to best reproduce the SLD profile with the smallest possible

number of free parameters. By fitting the reflectivity curves, nuclear and magnetic depth profiles of the FeRh layers were obtained, as shown in Fig. 3.9. In the as-grown sample measured in the AF state at 300 K, an enhanced magnetic moment was observed near the FeRh/MgO interface. Such an interfacial FM layer is typical for FeRh thin films as discussed in detail in Section 1.1. A weak magnetic contribution was also distributed throughout the FeRh layer with a small increase at the sample surface.
The H^+-irradiated sister sample H3 shows a similar overall magnetic depth profile. The interfacial magnetic contribution remains present, but with slight increase in its roughness at the neighboring FeRh sublayer and a reduced near-surface contribution compared to sample H2 is reduced. Since SRIM simulations predict a relatively uniform vacancy distribution for 20 keV H^+ irradiation, this behavior may indicate that irradiation-induced defects weakly enhance the FM contribution throughout the FeRh layer rather than creating a sharply localized FM region, smearing of the magnetic interfaces.
After C^+ irradiation, the residual magnetization increases strongly, reaching approximately 500 kA m^{-1} (Fig 3.8b). This increase is also reflected in the PNR-derived magnetic SLD profile, where the magnetic contribution is enhanced across the FeRh layer, with an additional increase close to the upper interface. This near-surface enhancement is qualitatively consistent with the SRIM vacancy profile for 20 keV C^+ irradiation, which predicts a broad damage distribution with a larger defect concentration closer to film surface. The data therefore suggest that C^+ irradiation stabilizes a residual FM contribution throughout the film, with a stronger effect in the near-surface region.

3.5 Phase-domain evolution after H^+ irradiation

The depth-dependent character of the phase transition is not known and may be influenced by strain gradients, defect distribution, epitaxial strain relaxation, interfacial effects, or by the residual magnetization localized near the substrate interface, as discussed in the previous section. In this section, we focus on two sister samples, H2 and H3, where sample H3 was irradiated with H^+ ions and sample H2 was kept in the as-grown state as a reference. The aim is to compare the phase-domain nucleation and propagation in the pristine and irradiated samples. The epitaxial strain is expected to be strongest near the substrate interface, which could locally delay the AF–FM transition and lead to the nucleation of the FM phase closer to the film surface. On the contrary, the residual ferromagnetic contribution at the interface could stabilize the FM phase locally and promote the onset of the transition near the substrate. The PNR could help us to clarify these questions. Another question is how ion irradiation modifies the phase domains.
Both samples were measured by PNR on superADAM in an external magnetic field of 500 mT. In this case, the measurements were performed at several temperatures corresponding to characteristic points of the thermal hysteresis, specifically the AF state, the phase-coexistence region during heating, the FM state, and the phase-coexistence region during cooling (see Fig 3.10).

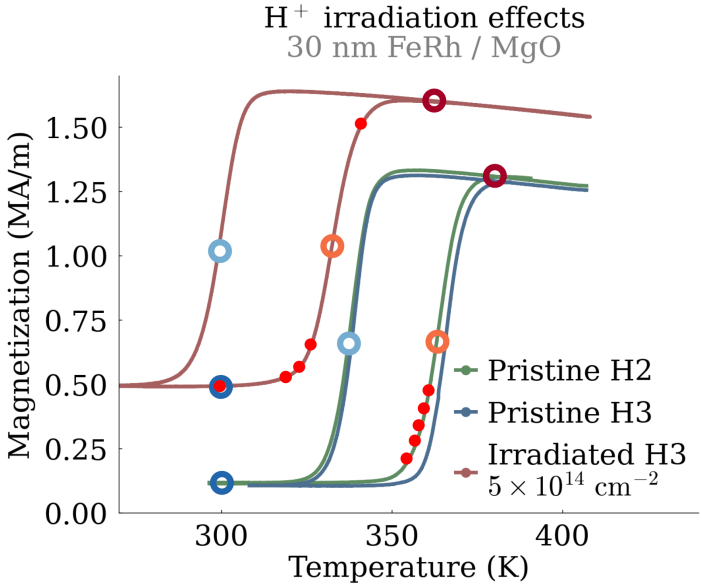


Figure 3.10: Thermal hysteresis of 30-nm-thick FeRh films grown on MgO. Two as-grown samples, H2 and H3, show very similar thermal hysteresis. The thermal hysteresis of sample H3 after 20 keV H^+ irradiation is shifted to lower temperatures. The empty circles indicate the temperatures at which the PNR measurements were performed. The red points indicate the temperatures at which the MFM measurements were performed.

For the as-grown sample H2, the PNR measurements yielded good fits with reasonably low figures of merit, as shown in Fig. 3.11. The comparison of the magnetic SLD profiles reveals a gradual evolution of the magnetic depth profiles during the phase transition. At 303 K, where the sample is in the AF state, only the residual magnetic contribution near the FeRh/MgO interface is observed. At 360 K, in the phase-coexistence region during heating, the magnetic SLD increases significantly. The strongest increase appears close to the MgO interface, which could suggest that the FM phase initially nucleates near the substrate. However, since this increase in magnetic moment remains in the fully FM phase at the temperature at 380 K, it rather indicates that the interface retains a larger magnetic moment than the rest of the FeRh layer.
During cooling, a small decrease in the magnetic SLD is observed near the surface at 334 K, which may suggest that the AF phase starts to form from the surface side. The nuclear SLD profiles show slight surface oxidation for all measured states, most likely due to the absence of a Pt capping layer. Overall, the magnetic SLD increase at 360 K and 380 K at the interface, together with the reduced magnetic SLD near the surface during cooling, suggests that the FM phase is more stable in the bottom part of the FeRh layer. The depth profiles of the H^+-irradiated sample H3 differ only slightly from those of the pristine H2 sample. The irradiated sample shows more prominent reduction in the magnetic SLD close to the surface, while the enhanced magnetic moment near the interface is less pronounced.
The increase in magnetization after irradiation, measured by VSM and shown in Fig. 3.10, is in line with the magnetic depth profiles as the magnetic SLD of H3 is noticeably higher than that of the pristine H2 sample.

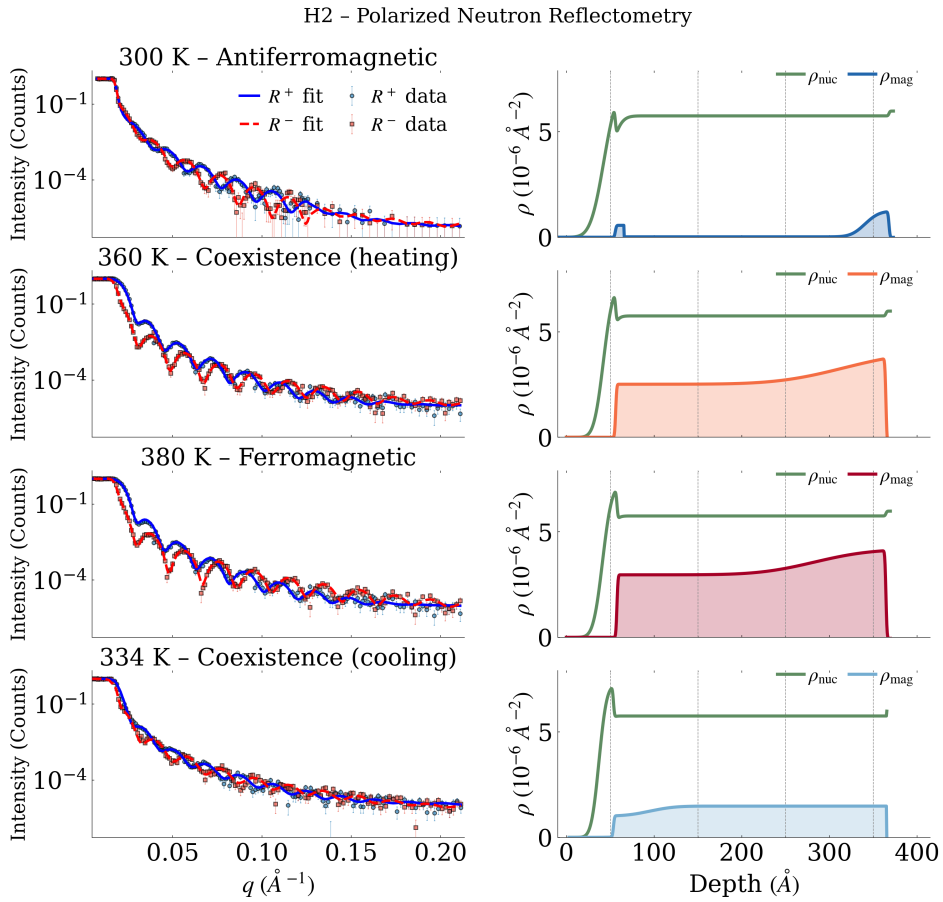


Figure 3.11: PNR results for the as-grown sample H2, measured at four characteristic temperatures: 303 K in the AF state, 360 K in the phase-coexistence region during heating, 380 K in the FM state, and 334 K in the phase-coexistence region during cooling. The left column shows the measured spin-up and spin-down reflectivity curves together with their fits. The right column shows the corresponding nuclear and magnetic SLD profiles in the right column. The figures of merit are 0.076, 0.083, 0.095, and 0.092, respectively.

MFM measurements revealed a significant difference in the lateral size of the phase domains. Figure 3.15 shows the phase-domain nucleation during heating. Within the investigated temperature range, clear nucleation of the FM domains is observed, while pronounced domain growth is not yet visible. For the pristine H2 sample at 361 K, the domain density is already high, and domain merging probably starts to dominate. This temperature is slightly below the transition point at which the phase-coexistence state was measured by PNR during heating. At this stage, the sample is likely already in the domain growth or merging regime, and the phase domains may extend through the full FeRh layer thickness. This is also supported by the fact that the lateral domain size in H2 reaches hundreds of nanometres, whereas the layer thickness is only approximately 30 nm. More pronounced depth-dependent variations could be expected at an earlier nucleation stage, which is observed by MFM at 357 K and 359 K for H2, and at 323 K and 326 K for H3.

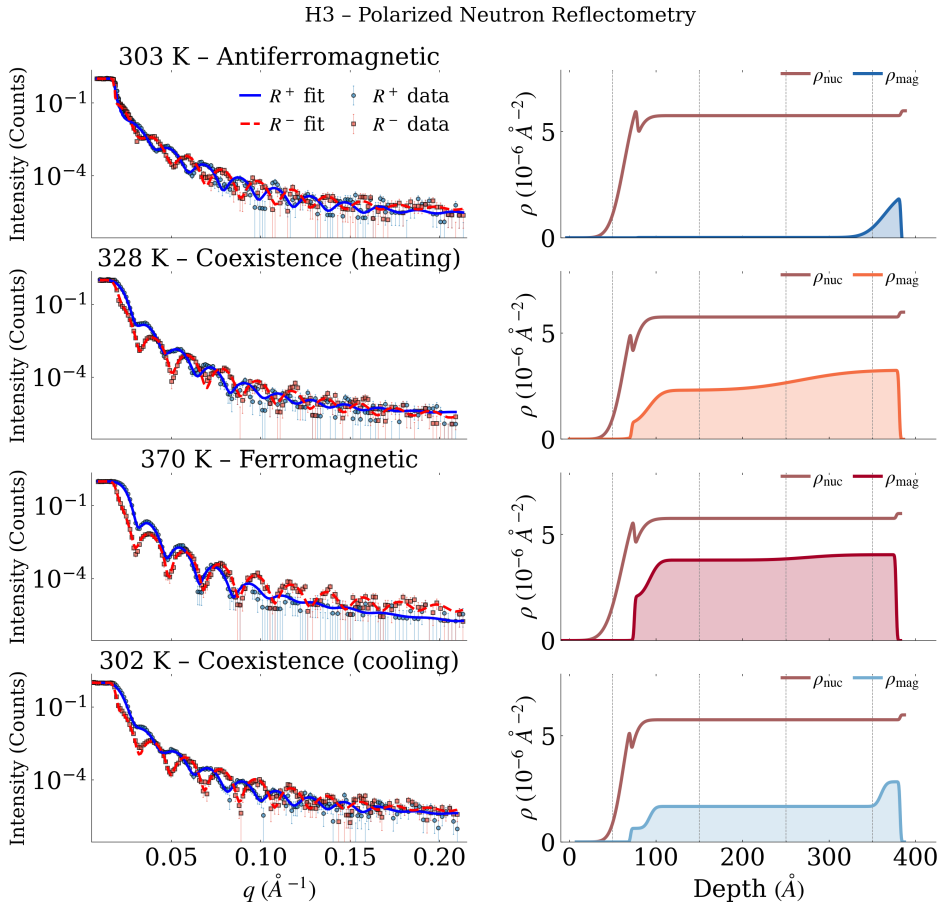


Figure 3.12: PNR results for the as-grown sample H3, measured at four characteristic temperatures: 303 K in the AF state, 328 K in the phase-coexistence region during heating, 370 K in the FM state, and 302 K in the phase-coexistence region during cooling. The left column shows the measured spin-up and spin-down reflectivity curves together with their fits. The right column shows the corresponding nuclear and magnetic SLD profiles in the right column. The figures of merit are 0.117, 0.125, 0.142, and 0.096, respectively.

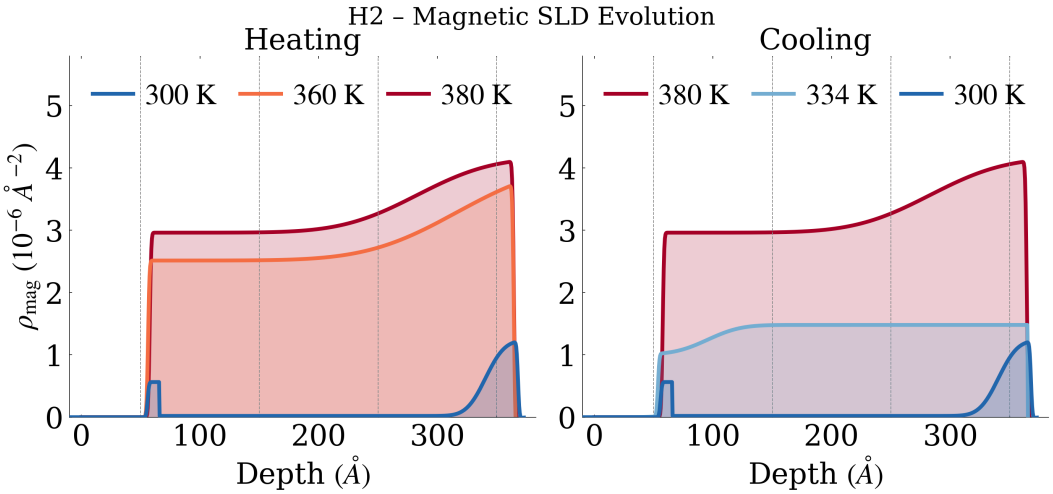


Figure 3.13: Comparison of the magnetic SLD profiles of the as-grown sample H2, showing gradual evolution of the magnetic depth profiles at selected temperatures upon heating and cooling across the phase transition. At 303 K, only the residual interfacial magnetization is present. At 360 K, the magnetic SLD increases significantly, with a stronger contribution near the substrate. This enhanced interfacial contribution persists in the FM state at 380 K. During cooling at 334 K, no enhanced surface contribution is observed. Instead, a slight reduction of the magnetic SLD near the surface is present.

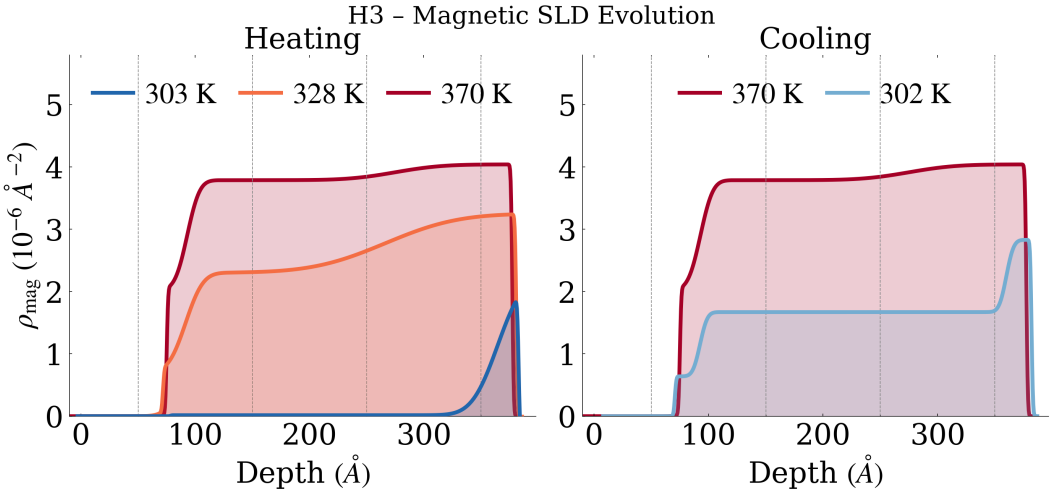


Figure 3.14: Magnetic SLD profiles of the H^+-irradiated sample H3 during heating and cooling across the phase transition. All profiles show a reduction of the magnetic SLD close to the sample surface, while an enhanced magnetic contribution near the substrate interface is again observed in both the phase-coexistence regions and in the fully FM state.

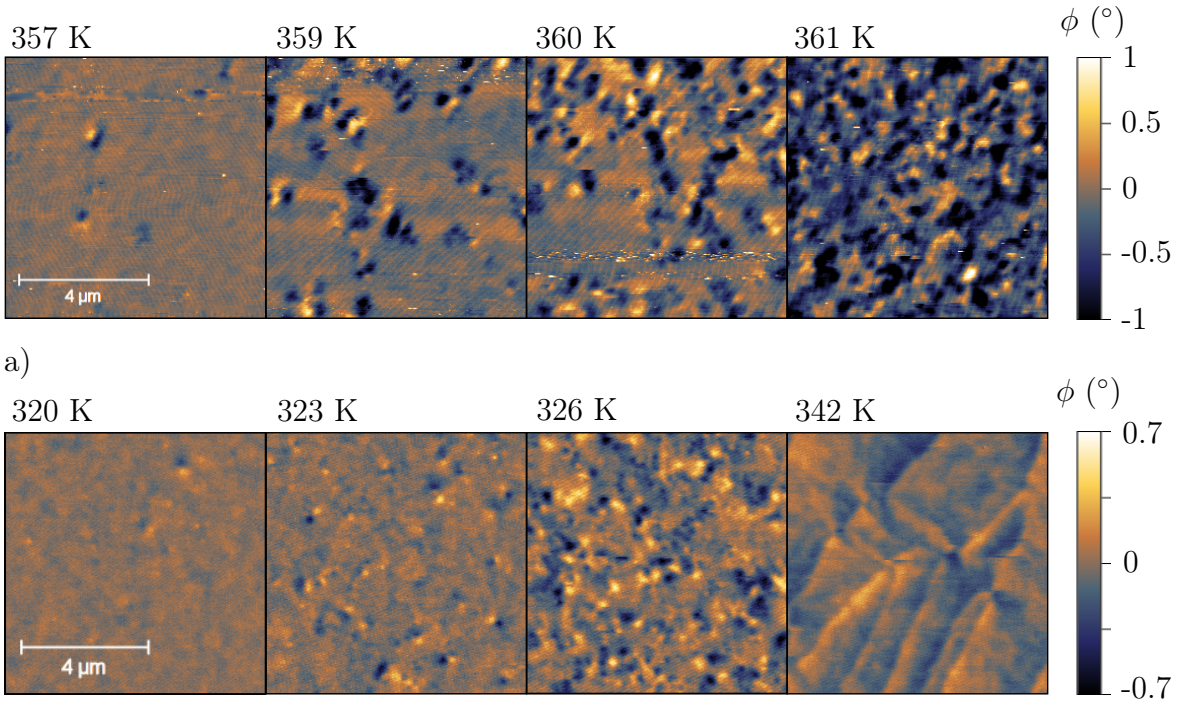


Figure 3.15: MFM images measured with a lift height of 100 nm, showing phase-domain nucleation during heating of the pristine H2 sample in the upper row and the H^+-irradiated H3 sample in the lower row. The domains are significantly smaller in the irradiated sample.

Conclusions

Within this work, the tunability of the phase transition in FeRh thin films was investigated by optimizing the deposition conditions and by subsequent irradiation with C^+ and H^+ ions with the energy of 20 keV. The study focused on controlling the transition temperature T_t, the hysteresis width ΔT, and the residual magnetization M_{res} through variations in film thickness, substrate, ion fluence, and irradiation temperature. The main objective was to find a suitable combination of parameters and obtain thermal hysteresis centered around room temperature with the largest width possible and minimal residual magnetization.

The results show that the thermal hysteresis of FeRh thin films can be significantly tuned already during deposition. The substrate has a strong influence on the transition temperature. Films grown on Al_2O_3 exhibit systematically lower T_t than films grown on MgO under otherwise comparable conditions. This behavior is consistent with the tensile strain component associated with Al_2O_3, which stabilizes the FM phase and shifts the transition to lower temperatures. At the same time, Al_2O_3 also tends to broaden the thermal hysteresis. Film thickness provides an additional tuning parameter. A reduction of the FeRh thickness leads to a decrease in T_t and to a broadening of the hysteresis. This trend cannot be explained by epitaxial strain alone, because the finite-thickness itself impacts the FeRh transition.

The reproducibility of the transition parameters was found to be strongly affected by the strain state of the film. The comparison of samples prepared with different substrate clamps indicates that even the mechanical mounting of the substrate during deposition can modify the FeRh lattice parameter and significantly affect the thermal hysteresis. Therefore, reliable tuning of FeRh during deposition requires not only control of the substrate and film thickness, but also careful control of sample mounting.

The most suitable sample from the present deposition series was sample consisting of a 20 nm-thick FeRh film grown on Al_2O_3 at an Ar sputtering pressure of 2.7×10^{-3} mbar. This sample exhibited a transition close to room temperature, with $T_t = 312$ K, a thermal hysteresis width of $\Delta T = 59$ K, and a residual magnetization of $M_{res} = 15\,\%$.

In addition to deposition tuning, ion irradiation was investigated as a post-deposition method for optimizing the FeRh thermal hysteresis. Irradiation with 20 keV C^+ ions proved to be an effective way to broaden the hysteresis, reaching up to $\Delta T = 84$ K. However, this maximum broadening was accompanied by a large decrease in T_t down to 227 K and by an increase in M_{res} up to 40 %. By selecting a suitable ion fluence, it was possible to obtain a thermal hysteresis located close to room temperature with a width of 56 K. Irradiation at elevated temperature, as well as post-irradiation annealing,

provided alternative approaches for optimizing the hysteresis. These methods reduced the excessive downward shift of T_t while preserving a broad transition, resulting in hysteresis widths of approximately 50 K close to room temperature. A comparison of the different approaches used for thermal hysteresis optimization is summarized in Table 3.1.

Table 3.1: Comparison of transition parameters obtained for selected tuning approaches. The irradiation was conducted with C^+ the energy of 20 keV. Both the irradiation at elevated temperature and the post-irradiation annealing were performed at 470 K.

	Deposition	Irradiation	Irradiation at elevated temperature	Irradiation and post-annealing
Dose (cm^{-2})	–	5×10^{12}	1.7×10^{13}	8×10^{12}
T_t (K)	312	306	312	312
ΔT (K)	59	56	55	48
M_{res} (%)	15	5	25	5

The investigation of residual magnetization revealed that, in the as-grown samples, the majority of the residual magnetic signal was localized at the interface with the substrate, within a layer approximately 3 nm thick. The residual magnetization within the FeRh layer itself was negligible, with only a slight increase near the surface. In the C^+-irradiated sample, the depth profile showed that the ferromagnetic signal was distributed throughout the FeRh layer, with a noticeable enhancement near the surface interface. This behavior may be explained by the depth profile of irradiation-induced vacancies simulated using SRIM.

During heating, the phase-domain nucleation in the as-grown sample appeared to be relatively uniform across the film thickness, with an enhanced magnetic moment at the substrate interface. This interfacial enhancement persisted even in the fully FM phase. During cooling, the magnetization depth profile again showed a rather uniform distribution, but with a decrease in the average magnetic moment near the surface.

Irradiation with 20 keV H^+ ions led to an increase in the saturation magnetization, as confirmed by vibrating sample magnetometry and polarized neutron reflectivity. The transition temperature decreased by 35 K, the hysteresis width increased by 23 K, and the residual magnetization increased by 20 %. MFM revealed changes in the phase-domain nucleation and propagation. The irradiated sample contained a larger number of nucleation sites and smaller phase domains, suggesting possible deceleration in the phase-domain growth after irradiation. This may explain the broadening of the thermal hysteresis loop. The depth profiles of magnetization at measured temperatures appeared similar to the depth profiles of the pristine sample, but with a more pronounced decrease in the average magnetic moment just below the sample surface.

The nearly uniform depth profiles observed during phase coexistence may be related to the stage of the transition at which the measurements were performed. As shown by MFM, directly at the selected transition temperatures during both heating and cooling, the majority of the film was already in the domain-growth or domain-merging

stage. At this stage, the phase domains likely extended through the entire FeRh layer, resulting in a rather uniform magnetic depth profile. More significant differences in the depth profile might be observable at the initial stages of nucleation, when the first nuclei appear.

Overall, we obtained the thermal hysteresis with transition temperatures centered around 300 K with the transition widths from 48 K to 59 K using proper combination of the substrate, layer thickness, carbon irradiation dose, irradiation temperature and post-annealing. We also observed the domain nucleation and the depth profiles of magnetization on as-grown and irradiated samples.

Bibliography

[1] Yoseph Imry and Michael Wortis. Influence of quenched impurities on first-order phase transitions. *Phys. Rev. B*, 19:3580–3585, 1979.

[2] L. H. Lewis, C. H. Marrows, and S. Langridge. Coupled magnetic, structural, and electronic phase transitions in FeRh. *Journal of Physics D: Applied Physics*, 49(32):323002, jul 2016.

[3] J. S. Kouvel and C. C. Hartelius. Anomalous Magnetic Moments and Transformations in the Ordered Alloy FeRh. *Journal of Applied Physics*, 33(3):1343–1344, mar 1962.

[4] Jon Ander Arregi, Friederike Ringe, Jan Hajduček, Olena Gomonay, Tomáš Molnár, Jiří Jaskowiec, and Vojtěch Uhlíř. Magnetic-field-controlled growth of magnetoelastic phase domains in ferh. *Journal of Physics: Materials*, 6(3):034003, may 2023.

[5] Radhika Barua, Félix Jiménez-Villacorta, and L. H. Lewis. Predicting magnetostructural trends in ferh-based ternary systems. *Applied Physics Letters*, 103(10):102407, 09 2013.

[6] S. Cervera, M. Trassinelli, M. Marangolo, C. Carrétéro, V. Garcia, S. Hidki, E. Jacquet, E. Lamour, A. Lévy, S. Macé, C. Prigent, J. P. Rozet, S. Steydli, and D. Vernhet. Modulating the phase transition temperature of giant magnetocaloric thin films by ion irradiation. *Phys. Rev. Mater.*, 1:065402, Nov 2017.

[7] L. Benito, L. Clark, T. P. Almeida, T. A. Moore, D. McGrouther, S. McVitie, and C. H. Marrows. Sputter-engineering a first-order magnetic phase transition in sub-15-nm-thick single-crystal ferh films. *Phys. Rev. Mater.*, 4:123402, Dec 2020.

[8] Jon Ander Arregi, Ondřej Caha, and Vojtěch Uhlíř. Evolution of strain across the magnetostructural phase transition in epitaxial ferh films on different substrates. *Phys. Rev. B*, 101:174413, May 2020.

[9] K. M. Cher, T. J. Zhou, and J. S. Chen. Compositional effects on the structure and phase transition of epitaxial ferh thin films. *IEEE Transactions on Magnetics*, 47(10):4033–4036, 2011.

[10] A. Ceballos, Zhanghui Chen, O. Schneider, C. Bordel, Lin-Wang Wang, and F. Hellman. Effect of strain and thickness on the transition temperature of epitaxial ferh thin-films. *Applied Physics Letters*, 111(17):172401, 10 2017.

[11] C. Bull, C. W. Barton, W. Griggs, A. Caruana, C. J. Kinane, P. W. Nutter, and T. Thomson. Pnr study of the phase transition in ferh thin films. *APL Materials*, 7(10):101117, 10 2019.

[12] G. C. Han, J. J. Qiu, Q. J. Yap, P. Luo, D. E. Laughlin, J. G. Zhu, T. Kanbe, and T. Shige. Magnetic stability of ultrathin ferh films. *Journal of Applied Physics*, 113(17):17C107, 03 2013.

[13] L. J. Swartzendruber. The FeRh (Iron-Rhodium) system. *Bulletin of Alloy Phase Diagrams*, 5(5):456–462, oct 1984.

[14] M Fallot and R Hocart. Sur l'apparition du ferromagnétisme par élévation de température dans des alliages de fer et de rhodium. *Rev. Sci*, 77:498, 1939.

[15] M. R. Ibarra and P. A. Algarabel. Giant volume magnetostriction in the ferh alloy. *Phys. Rev. B*, 50:4196–4199, Aug 1994.

[16] V. L. Moruzzi and P. M. Marcus. Antiferromagnetic-ferromagnetic transition in ferh. *Phys. Rev. B*, 46:2864–2873, Aug 1992.

[17] J. Kudrnovský, V. Drchal, and I. Turek. Physical properties of ferh alloys: The antiferromagnetic to ferromagnetic transition. *Phys. Rev. B*, 91:014435, Jan 2015.

[18] M Loving, F Jimenez-Villacorta, B Kaeswurm, D A Arena, C H Marrows, and L H Lewis. Structural evidence for stabilized ferromagnetism in epitaxial ferh nanoislands. *Journal of Physics D: Applied Physics*, 46(16):162002, apr 2013.

[19] C. Kittel. Model of exchange-inversion magnetization. *Phys. Rev.*, 120:335–342, Oct 1960.

[20] R. Y. Gu and V. P. Antropov. Dominance of the spin-wave contribution to the magnetic phase transition in ferh. *Phys. Rev. B*, 72:012403, Jul 2005.

[21] Joseph Barker and Roy W. Chantrell. Higher-order exchange interactions leading to metamagnetism in ferh. *Phys. Rev. B*, 92:094402, Sep 2015.

[22] C. W. Barton, T. A. Ostler, D. Huskisson, C. J. Kinane, S. J. Haigh, G. Hrkac, and T. Thomson. Substrate Induced Strain Field in FeRh Epilayers Grown on Single Crystal MgO (001) Substrates. *Scientific Reports*, 7(1):44397, April 2017.

[23] X. Z. Chen, J. F. Feng, Z. C. Wang, J. Zhang, X. Y. Zhong, C. Song, L. Jin, B. Zhang, F. Li, M. Jiang, Y. Z. Tan, X. J. Zhou, G. Y. Shi, X. F. Zhou, X. D. Han, S. C. Mao, Y. H. Chen, X. F. Han, and F. Pan. Tunneling anisotropic magnetoresistance driven by magnetic phase transition. *Nature Communications*, 8(1):449, sep 2017.

[24] Yeonbae Lee, Z. Q. Liu, J. T. Heron, J. D. Clarkson, J. Hong, C. Ko, M. D. Biegalski, U. Aschauer, S. L. Hsu, M. E. Nowakowski, J. Wu, H. M. Christen, S. Salahuddin, J. B. Bokor, N. A. Spaldin, D. G. Schlom, and R. Ramesh. Large resistivity modulation in mixed-phase metallic systems. *Nature Communications*, 6(1):5959, January 2015.

[25] Pampi Saha, Seema, V.R. Reddy, Pooja Gupta, Mukul Gupta, and R. Rawat. Effect of substrate and fe/rh stoichiometry on first order antiferromagnetic–ferromagnetic transition in ferh thin films. *Journal of Magnetism and Magnetic Materials*, 551:169095, 2022.

[26] Y. Ohtani and I. Hatakeyama. Features of broad magnetic transition in ferh thin film. *Journal of Magnetism and Magnetic Materials*, 131(3):339–344, 1994.

[27] M. P. Annaorazov, S. A. Nikitin, A. L. Tyurin, K. A. Asatryan, and A. Kh. Dovletov. Anomalously high entropy change in ferh alloy. *Journal of Applied Physics*, 79(3):1689–1695, 02 1996.

[28] S. Maat, J.-U. Thiele, and Eric E. Fullerton. Temperature and field hysteresis of the antiferromagnetic-to-ferromagnetic phase transition in epitaxial ferh films. *Phys. Rev. B*, 72:214432, Dec 2005.

[29] M. Jiang, X.Z. Chen, X.J. Zhou, Y.Y. Wang, F. Pan, and C. Song. Influence of film composition on the transition temperature of ferh films. *Journal of Crystal Growth*, 438:19–24, 2016.

[30] Jui-Chi Chung, Aswin kumar Anbalagan, Chen-Lin Fan, Yu-Hao Liao, Akhil K. Ramesh, Shivam Gupta, Yuan-Chieh Tseng, Nyan-Hwa Tai, and Chih-Hao Lee. Investigating the mechanism of magnetic phase transition temperature of ferh thin films by doping copper impurities. *Materials Chemistry and Physics*, 275:125252, 2022.

[31] J. B. Staunton, R. Banerjee, M. dos Santos Dias, A. Deak, and L. Szunyogh. Fluctuating local moments, itinerant electrons, and the magnetocaloric effect: Compositional hypersensitivity of ferh. *Phys. Rev. B*, 89:054427, Feb 2014.

[32] C. Baldasseroni, C. Bordel, A. X. Gray, A. M. Kaiser, F. Kronast, J. Herrero-Albillos, C. M. Schneider, C. S. Fadley, and F. Hellman. Temperature-driven nucleation of ferromagnetic domains in ferh thin films. *Applied Physics Letters*, 100(26):262401, 06 2012.

[33] Jiří Jaskowiec. Spatial confinement effects in metamagnetic nanostructures. Master's thesis, Brno University of Technology, Faculty of Mechanical Engineering, Brno, 2019. 55 pp. Supervised by Vojtěch Uhlíř.

[34] R. C. Temple, T. P. Almeida, J. R. Massey, K. Fallon, R. Lamb, S. A. Morley, F. Maccherozzi, S. S. Dhesi, D. McGrouther, S. McVitie, T. A. Moore, and C. H. Marrows. Antiferromagnetic-ferromagnetic phase domain development in nanopatterned ferh islands. *Phys. Rev. Mater.*, 2:104406, Oct 2018.

[35] S. Hrdinová. Vliv epitaxního napětí na koexistenci feromagnetické a antiferomagnetické fáze na bočním rozhraní mezi tenkou vrstvou a proužkem ferh. Bakalářská práce, Vysoké učení technické v Brně, Fakulta strojního inženýrství, Brno, 2024. 49 s. Vedoucí: Ing. Oleksii Zadorozhnii.

[36] Aleksei S. Komlev, Dmitriy Y. Karpenkov, Dmitry A. Kiselev, Tatiana S. Ilina, Alisa Chirkova, Radel R. Gimaev, Takamasa Usami, Tomoyasu Taniyama, Vladimir I. Zverev, and Nikolai S. Perov. Ferromagnetic phase nucleation and its growth evolution in ferh thin films. *Journal of Alloys and Compounds*, 874:159924, 2021.

[37] Thomas Coughlin. C4Q 2025 And 2025 Hard Disk Drive Industry Update, 2026. Digital Storage Technology & Market. IEEE President in 2024. Updated Feb 07, 2026.

[38] Seagate Blog. Three truths about hard drives and SSDs, may 2024. Data based on IDC Worldwide Global StorageSphere Forecast 2024-2028.

[39] H J Richter. The transition from longitudinal to perpendicular recording. *Journal of Physics D: Applied Physics*, 40(9):R149, apr 2007.

[40] M. Strungaru, B.T. Nguyen, K. Yuanmae, R.F.L. Evans, R.W. Chantrell, P. Chureemart, and J. Chureemart. Hamr switching dynamics and the magnetic recording quadrilemma. *Journal of Magnetism and Magnetic Materials*, 564:170041, 2022.

[41] Jan-Ulrich Thiele, Stefan Maat, and Eric E. Fullerton. Ferh/fept exchange spring films for thermally assisted magnetic recording media. *Applied Physics Letters*, 82(17):2859–2861, 04 2003.

[42] X. Marti, I. Fina, C. Frontera, Jian Liu, P. Wadley, Q. He, R. J. Paull, J. D. Clarkson, J. Kudrnovský, I. Turek, J. Kuneš, D. Yi, J-H. Chu, C. T. Nelson, L. You, E. Arenholz, S. Salahuddin, J. Fontcuberta, T. Jungwirth, and R. Ramesh. Room-temperature antiferromagnetic memory resistor. *Nature Materials*, 13(4):367–374, apr 2014.

[43] R. O. Cherifi, V. Ivanovskaya, L. C. Phillips, A. Zobelli, I. C. Infante, E. Jacquet, V. Garcia, S. Fusil, P. R. Briddon, N. Guiblin, A. Mougin, A. A. Ünal, F. Kronast, S. Valencia, B. Dkhil, A. Barthélémy, and M. Bibes. Electric-field control of magnetic order above room temperature. *Nature Materials*, 13(4):345–351, apr 2014.

[44] Leopold Palmetshofer. *Rutherford Backscattering Spectroscopy (RBS)*, chapter 11, pages 191–202. John Wiley Sons, Ltd, 2011.

[45] Matej Mayer. SIMNRA User's Guide. Technical Report IPP 9/113, Max-Planck-Institut für Plasmaphysik, Garching, Germany, 1997.

[46] Keisuke Yasuda. Time-Of-Flight ERDA for Depth Profiling of Light Elements. *Quantum Beam Science*, 4(4), 2020.

[47] K. Arstila, J. Julin, M.I. Laitinen, J. Aalto, T. Konu, S. Kärkkäinen, S. Rahkonen, M. Raunio, J. Itkonen, J.-P. Santanen, T. Tuovinen, and T. Sajavaara. Potku – New analysis software for heavy ion elastic recoil detection analysis. *Nuclear Instruments and Methods in Physics Research Section B: Beam Interactions with Materials and Atoms*, 331:34–41, 2014. 11th European Conference on Accelerators in Applied Research and Technology.

[48] Vojtěch Uhlíř, Federico Pressacco, Jon Ander Arregi, Pavel Procházka, Stanislav Průša, Michal Potoček, Tomáš Šikola, Jan Čechal, Azzedine Bendounan, and Fausto Sirotti. Single-layer graphene on epitaxial ferh thin films. *Applied Surface Science*, 514:145923, 2020.

[49] C.Q. Yu, H. Li, Y.M. Luo, L.Y. Zhu, Z.H. Qian, and T.J. Zhou. Thickness-dependent magnetic order and phase-transition dynamics in epitaxial fe-rich ferh thin films. *Physics Letters A*, 383(20):2424–2428, 2019.

[50] Sehwan Song, Chang woo Cho, Jiwoong Kim, Jisung Lee, Dooyong Lee, Doukyun Kim, Hyegyeong Kim, Haeyong Kang, Chul-Hong Park, Jun Kue Park, Jae Hyuck Jang, and Sungkyun Park. Correlation between phase transition characteristics and hydrogen irradiation-induced frenkel defect formations in ferh films. *Journal of Alloys and Compounds*, 901:163611, 2022.

[51] S. P. Bennett, A. Herklotz, C. D. Cress, A. Ievlev, C. M. Rouleau, I. I. Mazin, and V. Lauter. Magnetic order multilayering in ferh thin films by he-ion irradiation. *Materials Research Letters*, 6(1):106–112, 2018.

[52] James F. Ziegler, M. D. Ziegler, and J. P. Biersack. SRIM - The stopping and range of ions in matter (2010). *Nuclear Instruments and Methods in Physics Research B*, 268(11-12):1818–1823, jun 2010.

[53] Alexei Vorobiev, Jon Ander Arregi, A. N. Dobrynin, Sara Hrdinova, Victoria Kabanova, Yury Khaydukov, and Vojtech Uhlir. Investigation of localisation of ferromagnetic phases in thin FeRh films, 2026.

[54] C.F. Majkrzak, K.V. O'Donovan, and N.F. Berk. *Polarized Neutron Reflectometry*, pages 397–471. 12 2006.

[55] Artur Glavic and Matts Björck. *GenX 3*: the latest generation of an established tool. *Journal of Applied Crystallography*, 55(4):1063–1071, aug 2022.